ASTRONOMY & ASTROPHYSICS
SUPPLEMENT SERIES

Astron. Astrophys. Suppl. Ser. **132**, 211–231 (1998)

A survey of SiO emission towards interstellar masers

I. SiO line characteristics⋆

J. Harju[1], K. Lehtinen[1], R.S. Booth[2], and I. Zinchenko[3]

[1] Observatory, P.O. Box 14, FIN-00014 University of Helsinki, Finland
[2] Onsala Space Observatory, S-43992 Onsala, Sweden
[3] Institute of Applied Physics of the Russian Academy of Sciences, 46 Uljanov St., 603600 Nizhny Novgorod, Russia

Received July 3, 1997; accepted April 3, 1998

Abstract. We have conducted a survey of SiO emission towards galactic H_2O and OH masers and ultracompact HII regions using the 15-m SEST and the 20-m Onsala telescope. With the SEST the transitions ($v = 0, J = 2 - 1$) and ($v = 0, J = 3-2$) of SiO at 3 and 2 mm were measured simultaneously. With Onsala only the ($v = 0, J = 2 - 1$) line was accessible. Altogether 369 objects were observed and SiO was detected towards 137 of them. The detection rate is highest towards the most intense H_2O masers, which probably require powerful shocks to be excited. The SiO detection rate correlates also with the integrated far-infrared flux density and the FIR luminosity of the associated IRAS point source, indicating that the occurrence of shocks is related to the amount of radiation from the central stellar source(s). For flux and luminosity limited samples the SiO detection rate is higher in the inner 7 kpc from the galactic centre than elsewhere. This suggests that dense cores belonging to the so called "molecular ring" provide particularly favourable conditions for the production of gaseous SiO.

The full widths above 2σ of the SiO($J = 2 - 1$) lines, which are likely to be related to the associated shock velocities, range from 2 to 60 km s^{-1} except for the line in Ori KL which has a full width of about 100 km s^{-1}. The median of our sample is 19 km s^{-1}. The SiO lines are single-peaked and the peak velocities are always close to the ambient cloud velocity as determined from published CS observations. These line characteristics are compared with the predictions of kinematical bow-shock models. The SiO line shapes correspond with the model of Raga & Cabrit (1993) where the emission arises from turbulent wakes behind bow-shocks. However, the number of symmetric, relatively narrow profiles indicates that at least in some of the observed sources SiO emission arises also from the quiescent gas component.

We suggest that this is due to evaporation of silicon compounds from grain mantles and their reprocessing to SiO in dense quiescent gas according to the model of McKay (1995, 1996). These reactions may be initiated and sustained by ionizing radiation from shocks, in the same way as the enhancement of HCO^+ near Herbig-Haro objects has been explained in the model of Wolfire & Königl (1993).

The excitation temperatures of SiO($J = 2 - 1$) and ($J = 3 - 2$) transitions were determined towards three strong sources using measurements in isotopically substituted SiO. In all three sources the transitions are clearly subthermally excited, implying moderate densities ($< 3\,10^6$ cm^{-3}) in the SiO emission regions.

Key words: stars: formation — ISM: clouds — ISM: jets and outflows — ISM: molecules — radio lines: interstellar

1. Introduction

Thermal SiO emission in the ground vibrational state has been found to be associated with high-velocity flows and H_2O masers in massive star forming regions (Downes et al. 1982). In low-mass star-forming regions SiO emission comes exclusively from regions shocked by energetic outflows from young stellar objects and has very little or no contribution from the surrounding quiescent dense cores (e.g. Martín-Pintado et al. 1992; Bachiller 1996). The reason for this behaviour is that in cool dense gas SiO molecules are frozen onto dust grains. Si is however released in shocks due to evaporation of the grain mantles or destruction of their silicate cores, whereafter it quickly

Send offprint requests to: J. Harju

⋆ The entire Tables B.1 and B.2 and the spectra of all the detected SiO sources are only available in electronic form at the CDS via anonymous ftp to cdsarc.u-strasbg.fr (130.79.128.5) or via http://cdsweb.u-strasbg.fr/Abstract.html

reacts with O_2 or OH to form SiO (for recent chemical studies see McKay 1995, 1996 and Schilke et al. 1997).

Molecular masers originate from shock-energized dense gas in the neighbourhood of newly born massive stars. H_2O masers and Class I methanol (CH_3OH) masers are often associated with powerful molecular outflows (e.g. Felli et al. 1992; Menten 1991; Xiang & Turner 1995). In the model of Elitzur et al. (1989) H_2O masers form behind shocks produced when highly supersonic mass outflows from young stellar objects collide with clumps or inhomogeneities of the surrounding cloud. It seems, however, that also radiative pumping of H_2O masers is possible. Evidence for this in the case of a circumstellar accretion disk in S255 has been provided by Cesaroni (1990).

OH masers at 18-cm and Class II methanol masers are frequently seen in the direction or at the projected edges of ultra compact (UC) HII regions surrounding young massive stars (e.g. Gaume & Mutel 1987; Churchwell 1991; Menten et al. 1992). The required density enhancement for maser excitation in these regions may be caused by a bow-shock around the moving ionized shell (Van Buren et al. 1990). Recent interferometric observations have shown spatial-velocity structures indicative of rotation, thereby suggesting that also OH and CH_3OH masers can be associated with protostellar disks (Caswell 1997).

Although the various maser types probably occur in different physical regions, they can be spatially very close to each other (Forster & Caswell 1989; Forster et al. 1990). Therefore, besides theoretical investigation of the excitation requirements, observational studies of the maser kinematics and thermal emission from the associated shocks are important for the understanding of these phenomena.

It seems possible that the emission from rotational transitions of SiO near massive young stars comes from the regions where H_2O, OH and CH_3OH masers are excited. As a tracer of shocked gas, SiO is superior to the molecules often used in outflow studies, e.g. CO, CS, NH_3 and SO, since the emission is not confused by the ambient cloud component. With respect to maser emission, the advantage is the thermal (or quasi-thermal) nature, which does not exhibit rapid variations.

The purpose of the present survey is to find an extensive sample of strong SiO sources which could form a basis for more detailed studies of the structure, kinematics and thermal properties of the shock fronts associated with interstellar masers. In this paper we concentrate on the SiO detections and their line profiles, whereas in a subsequent paper we shall correlate the survey results with maser characteristics and with information inferred from the associated UC HII regions.

Previous observations suggest that SiO emission can arise from the cooling regions behind *bow shocks* (e.g. Dutrey et al. 1997). We therefore study the validity of the bow-shock hypothesis by comparing the SiO profiles with the predictions of kinematical models. An alternative related to the chemistry model of McKay (1995, 1996) is that SiO emission could come from dense clumps *irradiated* by powerful shocks (Wolfire & Königl 1993). In this latter case the lines are expected to be narrow.

In Sect. 2 of this paper, we give details of the target list selection criteria, and in Sect. 3 we describe the observations and the data analysis. The results from the observations are presented in Sect. 4. In Sect. 5 we discuss three bow-shock models and compare the predicted line profiles with the observations. Further discussion of the survey results is presented in Sect. 6. We conclude with a summary in Sect. 7.

2. Source selection

Our source list is mainly based on the Arcetri Atlas of galactic H_2O masers (Comoretto et al. 1990; Palagi et al. 1993; Brand et al. 1994; Arc), which covers the declination range $\delta > -30°$, and the catalog of non stellar H_2O/OH masers by Braz & Epchtein (1983, B&E). From the Arcetri Atlas we selected 174 H_2O masers which are associated with star forming regions. Some Arcetri sources have been included in our sample even though they are classified as late type stars (STAR) or of unknown type (UNKN) in Palagi et al. (1993). These sources have been detected in $CS(J = 7 - 6)$ by Plume et al. (1992) or in $NH_3(1, 1)$ by Molinari et al. (1996), and therefore probably are associated with star forming regions after all. In these cases the Palagi classification is indicated in brackets in Tables B.1 and B.2 described in Sect. 4.

From B&E we selected 60 H_2O masers which have declination $\delta < -30°$. The Arcetri and B&E lists were complemented by sources from the H_2O surveys of Henning et al. (1992, 17 sources), Scalise et al. (1989, 7 sources), Jenness et al. (1995, 6 sources), Braz et al. (1989, 5 sources) and Wouterloot & Walmsley (1986, 1 source, i.e. S152 OH2). Altogether the source list contains thus 270 H_2O masers. We started from the sources having H_2O maser peak flux densities greater than 10 Jy. When several observations are listed in the Arcetri Catalogue, we have taken the maximum of all observing rounds. In the course of the observations the flux density limit was relaxed in order to fill LST gaps. Of the selected H_2O masers, 55 (20 percent) have flux densities less than 10 Jy and 78 (29 percent) have flux densities greater than 100 Jy.

Many of the observed H_2O masers also exhibit OH and CH_3OH maser emission. Nineteen 18-cm OH maser sources *without* associated H_2O emission were included in the sample from B&E (originally from Caswell et al. 1983a,b and Caswell & Haynes 1983a,b) and the survey of Braz et al. (1990).

In addition to the masers, we observed 62 IRAS point sources fulfilling the colour criteria of ultracompact HII regions (Wood & Churchwell 1989). Except one (IRAS 18032-2032, SEST No. 145) these sources do not have any known H_2O masers closer than $30''$. The southern sources

(32) were selected directly from the IRAS point source catalogue. All except one are included in the CS survey of Bronfman et al. (1996). The northern sources were selected from the surveys of Molinari et al. (1996, 20 objects), Churchwell et al. (1990, 6 objects), and Bronfman et al. (1996, 4 objects).

Eleven dust continuum peaks within 40″ from H_2O masers detected in the survey of Jenness et al. (1995) and one location near the H_2O maser source S76E included in the CS(7−6) survey of Plume et al. (1992) were observed with Onsala in order to study the extension of SiO emission in these regions. In addition, during the Onsala runs altogether 6 positions towards the Herbig-Haro complexes HH1-3 (Haschick et al. 1983) and HH290 (Moreira & Yun 1995) were observed.

The total number of observed sources is 369. Three of them were observed with both SEST and Onsala. These sources are Ori KL (SEST No. 3, Onsala No. 40 in Tables B.1 and B.2, respectively), HH1-H_2O (SEST 6, Onsala 43) and NGC 2071 (SEST 11, Onsala 58). Our observing strategy was not intended to be unbiased. On the basis of a test survey we decided to start from the most intense H_2O masers in order to maximize the probability of detecting SiO, and thereby find suitable sources for further studies of shocked regions. The UC HII regions and OH masers were included to provide comparison material.

3. Observations and data analysis

3.1. SEST observations

The observations of the southern sources ($\delta < 0°$) were made during two periods in October 1995 and in April 1996, with the SEST[1] on La Silla in Chile. We measured the ($v = 0, J = 2-1$) and ($v = 0, J = 3-2$) transitions of SiO simultaneously, using the 80 − 116 GHz and 135 − 165 GHz SIS receivers. The backend was a 2000 channel acousto-optical spectrometer with a bandwidth of 86 MHz. The AOS was split in two bands, each of 43 MHz. The precise transition frequencies, the half-power beam widths (HPBW), and the antenna (η_A) and beam efficiences (η_{MB}) of the telescope are listed in Table 1. Also the Jy/K conversion factors assuming a point source, and the velocity resolutions corresponding to the channel separation at the frequencies 87 and 130 GHz are listed there. Further details of the equipment can be found in Booth et al. (1989) or in the SEST manual (see http://www.ls.eso.org/lasilla/Telescopes/SEST).

Typical system temperatures at 87 and 130 GHz were 130 and 160 K, respectively. The observations were made in the dual beam switching mode, with a beam throw of 11′.5. The pointing was checked by observing circumstellar SiO maser sources, and the accuracy was found to be better than 3″.

[1] SEST=Swedish–ESO Submillimetre Telescope.

3.2. Onsala observations

The northern sources ($\delta > 0°$) were observed in January 1995 and in March 1996 with the 20-m radio telescope of Onsala Space Observatory in Sweden. The SiO($v = 0, J = 2-1$) line was measured using a 3 mm SIS receiver. As backends we used both the autocorrelator with a resolution of 50 kHz, and the 256 channel filterbank of resolution of 250 kHz. The antenna parameters and the velocity resolutions of the spectrometers are listed in Table 1. For most of the sources the signal-to-noise ratio in the autocorrelator spectra was not high enough to study the line profiles at low intensity levels. On the other hand, the relatively low resolution of the filter-bank (0.86 km s^{-1} at the line frequency) is sufficient as the lines are typically broad. Therefore the analysis is based on the filter-bank spectra alone.

The first observing run was hampered by snow and rain, and consequently the system temperature varied between about 240−1000 K. During the second run, the typical system temperatures were between 300−400 K. The observing mode was dual beam switching with a beam throw of 11′.5. The focus and pointing was checked by observing SiO masers in late-type stars. The pointing accuracy was found to be better than 4″.

3.3. Determination of the line parameters

Because many of the spectra are asymmetric, gaussian fits are not applicable. Linear baselines were first subtracted from the spectra. Due to spectral noise it is difficult to determine the minimum and maximum velocities (V_{min}, V_{max} in Tables B.1 and B2) of the low-intensity line wings. Therefore the spectra were first smoothed by averaging adjacent channels in order to reduce the noise level.

The SEST spectra were smoothed by averaging 8 adjacent channels resulting in a velocity resolution of 1.2 and 0.79 km s^{-1} for the $J = 2-1$ and $J = 3-2$ transitions, respectively. In the Onsala spectra two adjacent channels were averaged and the resulting velocity resolution is 1.73 km s^{-1}. The smoothing lowers noise but also reduces the accuracy of the determined velocities. However, compared with the typical full widths of the lines as defined below, the obtained spectral resolution is reasonable.

The peak antenna temperatures and the corresponding velocities ($T_A^\star$ and V_{peak} in Tables B.1 and B.2) were determined directly from the smoothed spectra. The full velocity range of detectable emission, which hereafter will be called the full width (FW), was then determined as the range where the channel values are greater than twice the RMS noise of the smoothed spectra. Due to smoothing the selected intensity threshold corresponds to $T_{rms}/\sqrt{2}$ for the SEST observations and $T_{rms}\cdot\sqrt{2}$ for the Onsala observations, where T_{rms} is the RMS noise of the original spectra indicated in Tables B.1 and B.2. The area, mean

Table 1. Antenna and beam efficiences, the Jy/K conversion factor for a point source, and spectrometer resolutions for the 15-m SEST and the 20-m Onsala telescope at the observed frequencies

		15-m SEST					20-m Onsala					
transition	frequency (MHz)	HPBW ($''$)	η_A	$\eta_{\rm MB}$	Jy/K	$\Delta v_{\rm AOS}$ (km s^{-1})	HPBW ($''$)	$\eta_{\rm A}$	$\eta_{\rm MB}$	Jy/K	$\Delta v_{\rm FB}$ (km s^{-1})	$\Delta v_{\rm AC}$ (km s^{-1})
SiO(2−1)	86847.00	57	0.62	0.75	25	0.15	43	0.40	0.60	22	0.86	0.17
SiO(3−2)	130268.70	40	0.56	0.68	28	0.10	-	-	-	-	-	-

velocity and width (the columns Area, $V_{\rm mean}$ and Width in Tables B.1 and B.2, respectively) of the emission within the range $V_{\rm min} - V_{\rm max}$ were calculated using the original spectra. The mean velocity and width are defined as the first and second moments of the channel values.

4. Results

Our main results are given in tables and spectral figures, which are available in electronic form in the address given on the title page of this article. The tables contain the selected sources and the observed SiO line parameters. The associated H_2O maser line properties, when available in the Arcetri or B&E catalogues, are also included. The SEST and Onsala observations are listed separately, which results in two tables (B.1 and B.2), the first pages of which are shown in Appendix B. The entries are arranged according to increasing right ascension.

The columns of Tables B.1 and B.2 are: (1) source number, name, galactic coordinates (l, b) and distance, for detected sources the name is printed in boldface characters; (2) 1950.0 equatorial coordinates; (3) observed transition plus the reference of the maser catalogue (usually Arcetri (Arc.) or Braz & Epchtein 1983 (B&E)); (4) peak antenna temperatures $T_{\rm A}^*$ of the SiO lines (if detected) and the measured maximum flux density of the H_2O maser (or sometimes OH maser, in which case clearly indicated); (5) rms noise of the original SiO and the H_2O spectra; (6) peak velocities $V_{\rm peak}$ of the SiO lines and the velocity of the strongest maser component; (7) detected minimum velocities $V_{\rm min}$ of the SiO emission and maser features (when reliably determined and listed); (8) the corresponding maximum velocities $V_{\rm max}$; (9) velocity centroids $V_{\rm cen}$ of the SiO emission and maser features ($\equiv (V_{\rm min} + V_{\rm max})/2$); (10) intensity weighted average velocity $V_{\rm mean}$ for SiO; (11) full width (FW) of the detected SiO lines and maser emission features ($\equiv V_{\rm max} - V_{\rm min}$); (12) SiO line widths (variance or the second moment); (13) the integrated intensities of the SiO lines and the integrated flux density of the maser line (if available); (14) asymmetry parameter P of the SiO lines defined as $2\,(V_{\rm peak} - V_{\rm cen})/FW$, and the velocity of the associated molecular cloud ($V_{\rm cloud}$) found in the literature; (15) References to other surveys and association with a known object within $20''$. The key for the reference codes are given on the first pages of Tables B.1 and B.2. A reference is given without brackets if the positional coincidence is better than $5''$, and in brackets if the difference between the used coordinates is $5 - 20''$.

When no reference is given the distance in Col. (1) is a kinematic distance calculated from the cloud velocity given in Col. (14) by using the galactic rotation curve determined by Brand & Blitz (1993) for $R_0 = 8.5$ kpc and $\Theta_0 = 220$ km s^{-1}. For sources in the first and fourth quadrants with a distance ambiquity the near kinematic distance was assumed. The reference codes of photometric distances are explained in the bottom of the first page of each table. A hyphen (-) means that no solution has been found with the kinematical model, nor any reference to a photometric distance. The cloud velocity, $V_{\rm cloud}$, refers usually to the velocity of the associated dense core as estimated from CS data. When the latter has not been available, a radial velocity determined from NH_3 or CO observations has been used. The references are given below the distance references in Tables B.1 and B2. If no molecular line measurements has been found in the literature we have used for the kinematic distance estimate the peak radial velocity of the SiO($J = 2 - 1$) line from the present survey or the peak velocity of the associated maser. In this case the corresponding field in Col. (14) is empty.

All the detected SiO lines are presented in the spectral figures since the line shape changes considerably from source to source and contains information on the nature of the associated shock. The spectra can be identified with the entries of Tables B.1 and B.2 by the source number and name. The first nine detections (in order in the tables) of the SEST and Onsala surveys are shown in Appendix B.

The H_2O maser velocity ranges and the peak velocities from the Arcetri catalogue are indicated in the spectral figures. For H_2O masers with $\delta < -30°$ only the peak velocities are marked, which are available in B&E. For several southern sources the velocity range of the 18-cm OH maser features found in the literature is also indicated.

4.1. Detection rate

Table 2 indicates the detection rates with the SEST and the Onsala telescope for three different source categories: 1.3-cm H_2O masers, OH masers and IRAS sources with colours typical of ultracompact HII-regions.

Table 2. Numbers of observed H_2O masers, OH masers and UC HII regions and SiO detections with SEST and Onsala

	H_2O	OH	UC HII
SEST			
SiO(2−1)&(3−2)	136	16	32
detected	**74**	**5**	**17**
Onsala			
SiO(2−1)	137	3	30
detected	**37**	**0**	**1**
Σ detections	**109***	**5**	**18**

*Three H_2O maser sources were observed with both telescopes and two of them were detected.

In addition, SiO was detected with Onsala towards 3 of the 11 dust continuum emission peaks near H_2O masers from the survey of Jenness et al. (1996), and towards the CS(7−6) position in S76E from the survey of Plume et al. (1992). The total number of detections is 136. With the SEST the detection was always made in both $J = 2 - 1$ and $J = 3 - 2$ transitions, except towards the source No. 164 (OH19.48+0.16), where only $J = 2 - 1$ was detected. The intensity ratios of these two lines are discussed in a later section.

According to Table 2 there is a clear difference in the overall detection rates between the Onsala telescope and the SEST. Only 22 percent of the target sources were detected in SiO with Onsala, whereas the detection rate with SEST is 52 percent. The effective apertures and the achieved RMS noise levels are similar for both telescopes. It is conceivable, therefore, that the difference in detection rates is due to the properties of the selected target sources. In the following we shall discuss their galactic distribution, the flux densities of the associated H_2O masers, and the far-infrared flux densities and luminosities of the associated IRAS point sources.

The median values of the derived and adopted distances are 3.0 kpc and 3.3 kpc for the SEST and Onsala samples, respectively. The lower detection rate with Onsala is therefore not caused by the fact that the target sources would be on the average further away.

In Fig. 1, the detection rate as a function of the galactic longitude is graphed as a histogram showing the number of observations and detections for 30° wide intervals. The longitude ranges covered by the SEST and Onsala observations are indicated. The SEST target sources are mostly concentrated to the galactic plane, whereas the sources observed with Onsala have larger scatter in the galactic latitude. This can be seen by comparing the histograms in Fig. 1a, which represents all observed and detected sources, and in Fig. 1b, where only sources within 2° from the galactic plane are included. It is evident from both figures, that the detection rate is the highest in the galactic longitude range $300° \leq l < 30°$. Outside this range there is no great difference between the detection rates with Onsala and the SEST.

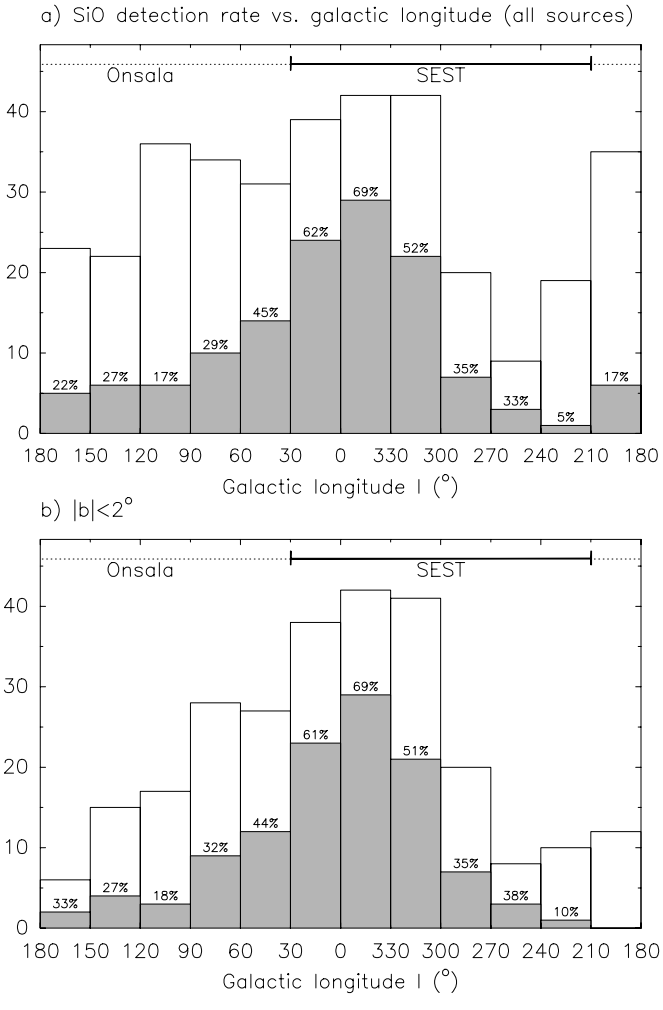

Fig. 1. Number of observed sources and SiO detections as a function of the galactic longitude **a)** for all sources and **b)** for sources within 2° from the galactic plane. The longitude ranges covered by the SEST and Onsala observations are indicated

The projected distribution of the observed and detected sources in the galactic plane is shown in Fig. 2. The SEST and Onsala target sources are denoted by different markers. The solar circle and a circle with a radius of 3 kpc are indicated in the figure. The latter circle roughly corresponds to the inner boundary of the so called "molecular ring" between galactocentric distances 3 and 7 kpc with a large H_2 surface density as determined from CO observations (Dame et al. 1987; Blitz 1997). Almost all sources (96%) in the sector defined by $330° \leq l \leq 30°$ belong to the "molecular ring" and the percentage is high (73%) also in the neighbouring 30° wide sectors i.e. $300° \leq l < 330°$ and $30° < l \leq 60°$. The average galactocentric distances in these regions are 5.5 kpc ($|l| \leq 30°$) and 6.5 kpc ($30° < |l| \leq 60°$).

The distribution of the detection rate as a function of the galactocentric radius is plotted in Fig. 3. All H_2O and OH masers and IRAS sources with colours typical of UC

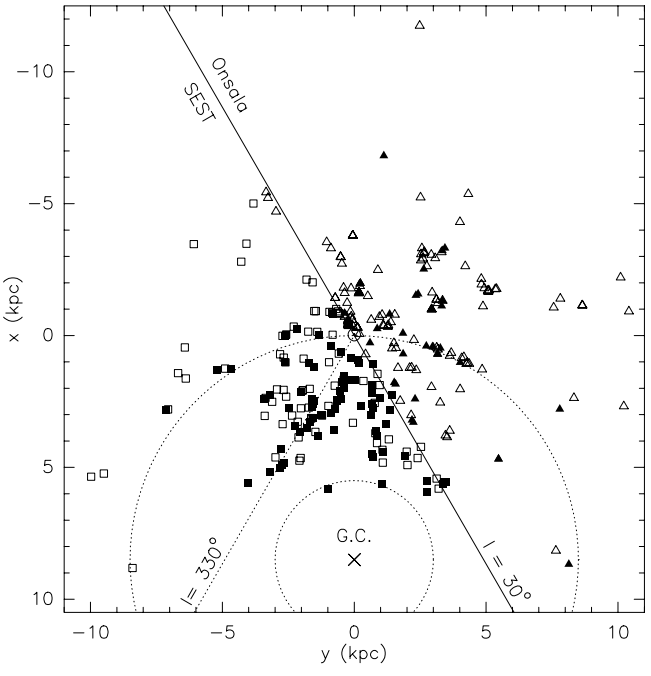

Fig. 2. A "face-on" view of the distribution of the observed and detected sources. The SEST survey objects are denoted by squares and the Onsala survey objects are denoted by triangles. Filled markers indicate detections. The locations of the sun and the galactic centre are denoted by $\odot$ and a cross, respectively. The SEST survey covers the half-plane from $l = 210°$ to $l = 30°$. The direction $l = 330°$ is denoted by a dashed line. The solar circle and the galactocentric radius 3 kpc are also indicated

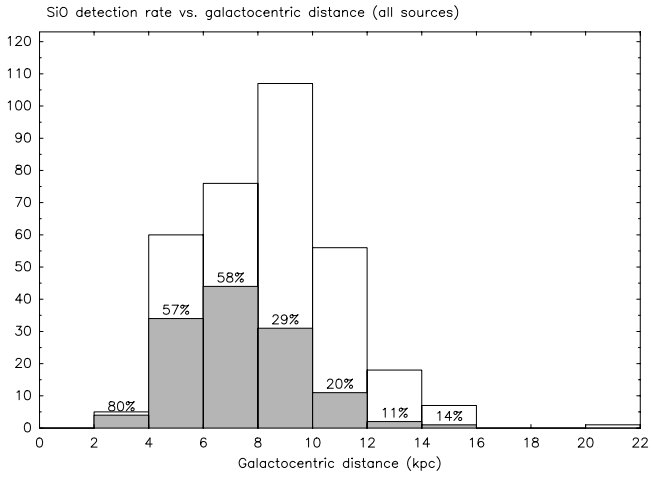

Fig. 3. Number of observed and detected sources as a function of the galactocentric radius. All masers and IRAS sources fulfilling the colour criteria of UC HII regions are included

HII regions are included. It can be seen in this figure that the detection rate is higher among sources within the solar circle than for those located in the outer Galaxy.

Examination of the individual source properties reveals that the detection rate is the highest towards intense H_2O masers. This tendency is illustrated in Fig. 4, which shows a histogram of the detection rate as a function of H_2O maser peak flux density. For Arcetri sources the maximum H_2O flux density has been taken in case several measurements are listed. One can see in the diagram that the detection percentage is about 60 or higher when the maser peak flux density exceeds 100 Jy. The Onsala sample contains 40 masers with peak flux densities less than 10 Jy, whereas with SEST only 15 such masers were observed. The median values of $\log F_{\mathrm{H_2O}}$ are 1.78 and 1.45 for the H_2O masers observed with SEST and Onsala, respectively. This corresponds to a difference by a factor of two in the flux density. The variability of H_2O masers complicates the interpretation of these results. The flux densities of some sources may have changed by one or even two orders of magnitude after the catalogued measurements, and it is uncertain whether Fig. 4 represents a real correlation.

The H_2O maser luminosity has been found to be related to the far-infrared luminosity of the associated IRAS Point Source Catalogue (PSC) objects (Wouterloot & Walmsley 1986). In their survey of a large sample of IRAS sources, Wouterloot et al. (1995) arrived at the conclusion that the observed maximum H_2O maser luminosity at a certain FIR luminosity is proportional to L_{FIR} of the associated IRAS source (see their Fig. 8).

Most H_2O masers in our sample are associated with IRAS point sources. According to the results of Wouterloot et al. (1995) the FIR flux density of an IRAS source could give an estimate for the upper limit of the integrated flux density of the associated H_2O maser at any time. We have therefore plotted in Fig. 5a a histogram of SiO observations and detections as a function of the logarithm of the integrated FIR flux density (F_{FIR} [$\mathrm{Wm^{-2}}$]) for all IRAS point sources, which are located within a radius of 25″ from the survey positions, and have "maser-like" colours as determined by Wouterloot & Walmsley (1986) or have typical colours of UC HII regions as determined by Wood & Churchwell (1989). The integrated FIR flux density between 7 and 135 μm has been calculated by using the method of Emerson (1988). In Fig. 5b a similar histogram is presented for FIR luminosities (L_{FIR} [$L_\odot$]), calculated by using the distances given in Tables B.1 and B.2. Due to large overlap in the colour-colour diagrams of the associated IRAS sources and the observed spatial intermixing of H_2O masers and UC HII regions we have not distinguished here between the two object categories. The total number of selected IRAS sources is 206, out of which 137 (67%) fullfill both colour criteria.

One can see in Fig. 5a that the SiO detection rate is higher in the neighbourhood of IRAS point sources with large FIR flux densities, and exceeds 50% in the range $-9.5 < \log F_{\mathrm{FIR}} < -8.5$. According to Fig. 5b the detection rate is 40 percent or higher for sources with FIR luminosity higher than 4 solar luminosities.

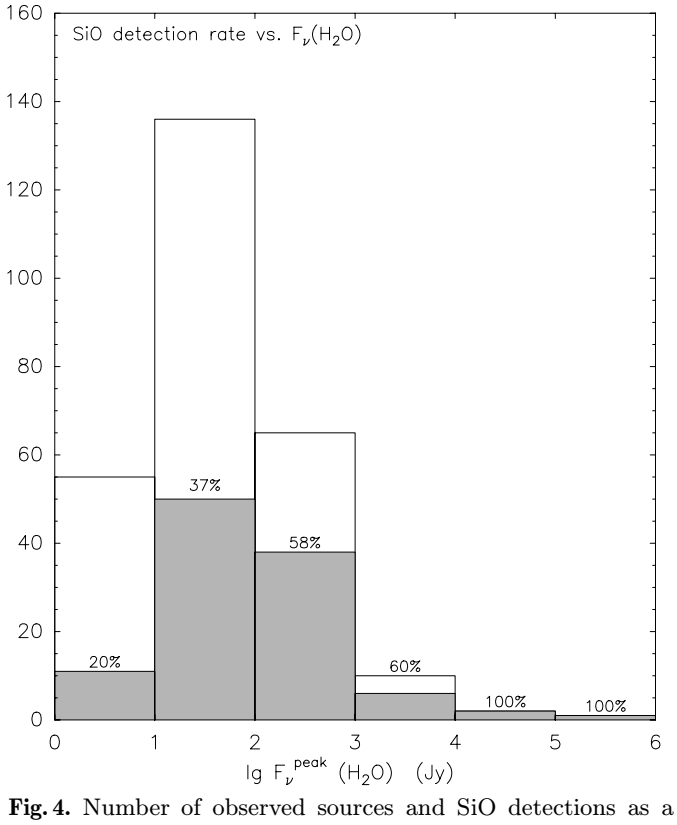

Fig. 4. Number of observed sources and SiO detections as a function of the H_2O maser peak flux density in Jy. Both Onsala and SEST survey objects are included

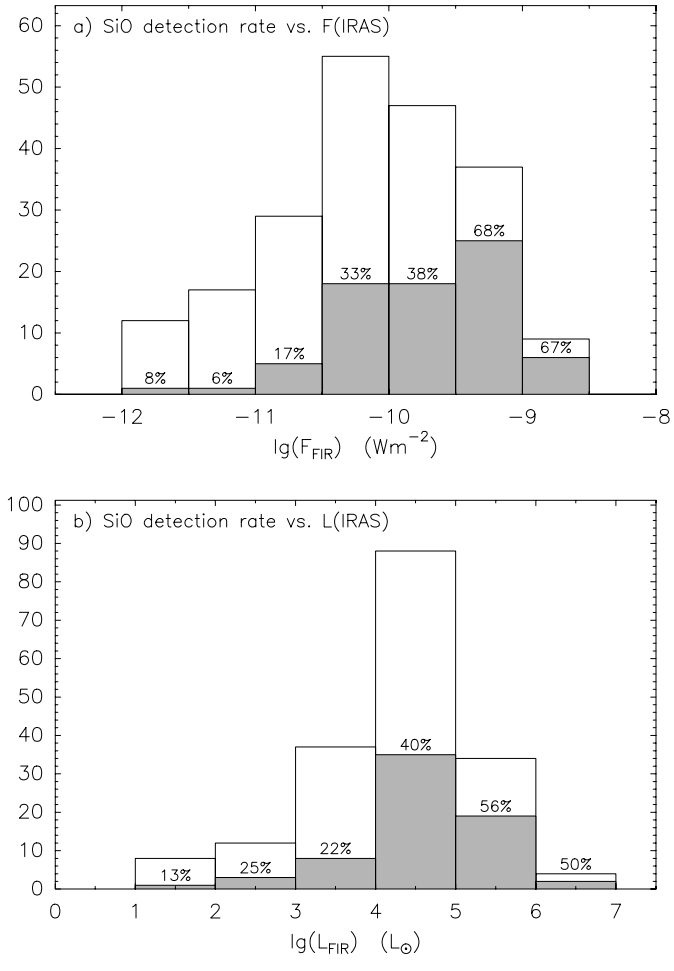

Fig. 5. Number of observed sources and SiO detections **a)** as a function of the integrated FIR flux density (Wm^-2) and **b)** the FIR luminosity ($L_\odot$) of the associated IRAS point source. The point sources selected to the latter histogram have "maser-like" or "UC HII-like" colours (see text). The positional coincidence required is 25″ or better. Both Onsala and SEST survey objects are included in these diagrams

The correlation with the FIR luminosity is, however, less marked than in the case of the flux density. This is probably due to the fact that the SiO emission regions are relatively compact and their detection becomes more difficult with increasing distance. It should be noted furthermore that the uncertainties of the distance estimates may cause errors in the derived luminosities.

The minimum and maximum FIR flux density and luminosity are similar for the SEST and Onsala samples. However, the SEST sample contains more bright IRAS sources. The median values of $\log F_{\rm FIR}$ are -9.72 and -10.45 and the median values of $\log L_{\rm FIR}$ are 4.76 and 4.19 for the SEST and Onsala samples, respectively. The difference by a factor of 5 in the FIR flux density is particularly noteworthy. A closer look at the distribution of the IRAS sources shows that 54 percent of the IRAS sources with $\log F_{\rm FIR} > -10$ are located in the galactic longitude range $300^\circ \leq l \leq 0^\circ$, which contains 32 percent of the 206 selected IRAS sources.

The fact that the detection rate is higher towards bright IRAS sources suggests that the intensity of SiO emission is correlated with the thermal FIR emission from circumstellar dust around the associated young stellar object. On the other hand, the detection rate is higher for objects lying between the galactocentric distances 3 and 7 kpc (roughly sources in the galactic longitude range $300^\circ \leq l \leq 60^\circ$) than those located further away from the galactic centre. This region has a high molecular gas surface density and contains a large concentration of HII regions and embedded massive stars (e.g. Bronfman 1992; Blitz 1997). Due to a large number of sources in the corresponding part of the sky and the fact that we started from the brightest H_2O masers and IRAS sources the final sample there contains a high fraction of probable SiO emission sources.

Is the higher detection rate for the sources belonging to the "molecular ring" then a selection effect? In order to examine this we have plotted the SiO detection percentage as a function of the galactic longitude including only objects which are associated with *bright*

IRAS point sources. Figure 6a represents sources with $\log F_{\rm FIR} > -10.5$, whereas in Fig. 6b the detection rate is plotted for sources with $\log L_{\rm FIR}/L_\odot > 4$. The total number of sources falling within each 60° wide interval is indicated in the lower left corner of the respective column. The errors have been estimated by assuming that the probability for detecting any specific number of sources in a certain longitude range is given by the binomial probability function. The histogram of the luminosity limited sample in Fig. 6a suggests that the detection rate is higher in the longitude range $300° \leq l < 60°$ than elsewhere, except perhaps the longitude range $240° \leq l < 300°$, where the relative error is rather large, however. The high detection rate in the latter interval is probably influenced by the fact that between $l = 280°$ and $l = 300°$ we are looking along the Sagittarius-Carina arm (Georgelin & Georgelin 1976). The average detection rate within $300° \leq l < 60°$ for the luminosity limited sample is $61 \pm 6\%$, whereas for the other two equal intervals of longitude the detections rates are $33 \pm 10\%$ ($180° \leq l < 300°$) and $23 \pm 7\%$ ($60° \leq l < 180°$). The corresponding averages for the flux limited sample are similar. It seems thus that the higher detection rate amongst the sources belonging to the "molecular ring" cannot be solely explained by the fact that the selected target sources there are associated with brighter FIR sources.

4.2. Line profiles

The distribution of the full widths above twice the RMS noise of the SiO($J = 2-1$) lines is presented as a histogram in Fig. 7. The velocity extent of the emission ranges from 2 to 60 km s^{-1}, except for Ori KL where the line has a full width of 103 km s^{-1}. The median value of the full width is 19 km s^{-1}.

In addition to their width the line shapes are described in Tables B.1 and B.2 by their symmetry or asymmetry with respect to the peak. We define an asymmetry parameter P as follows:

$$P \equiv \frac{V_{\rm peak} - V_{\rm cen}}{0.5\,(V_{\rm max} - V_{\rm min})}\,, \qquad (1)$$

where $V_{\rm cen} = (V_{\rm min} + V_{\rm max})/2$. The parameter P, which is twice the "normalized peak position or NPP" of Palagi et al. (1993), can have values from -1 to $+1$. $P = 0$ means that the line is symmetric. $P = -1$ and $P = +1$ correspond to cases where $V_{\rm peak} = V_{\rm min}$ and $V_{\rm peak} = V_{\rm max}$, respectively.

The distributions of the asymmetry parameter P of the SiO($J = 2-1$) and SiO($J = 3-2$) spectra obtained at SEST are shown in Fig. 8. Only SEST observations were selected for this presentation, since they are better suited to analysis of the line shapes due to their higher S/N ratio and spectral resolution.

For both transitions the P-values are heavily concentrated close to zero. The mean values and the sample standard deviations of P for the $J = 2-1$ and $J = 3-2$ lines

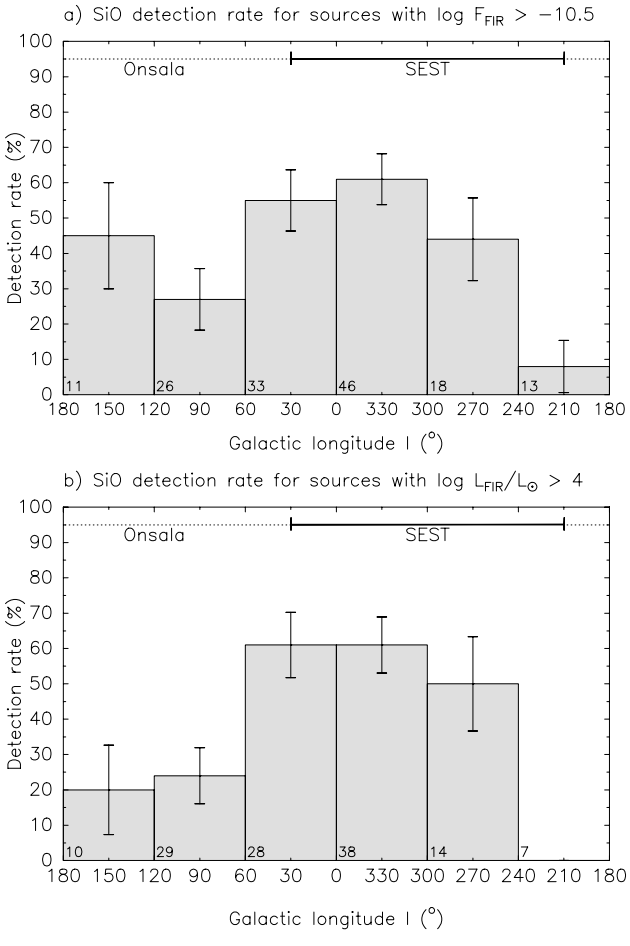

Fig. 6. SiO detection percentages as a function of the galactic longitude **a)** for sources with $\log F_{\rm FIR} > -10.5$ (Wm^{-2}) and **b)** for sources with $\log L_{\rm FIR}/L_\odot > 4$. The number in the lower left of each column gives the total number of selected sources in the corresponding galactic longitude range

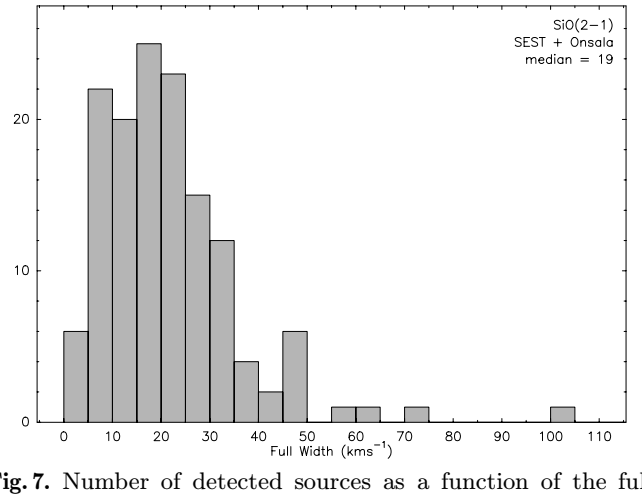

Fig. 7. Number of detected sources as a function of the full width above two sigma of the SiO($J = 2-1$) line. Both Onsala and SEST detections are included in the data

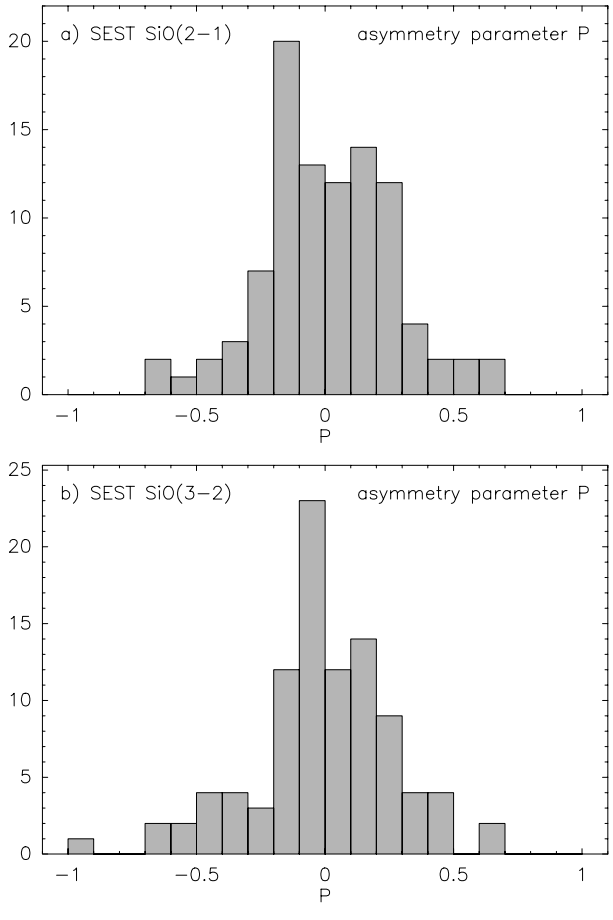

Fig. 8. Distribution of the asymmetry parameter P for the SiO($J = 2 - 1$) **a)** and SiO($J = 3 - 2$) **b)** spectra obtained with the SEST. The value $P = 0$ represents a symmetric line, a negative value corresponds to the case where the line peak is blueshifted with respect to the velocity centroid, and a posivite value indicates that the peak is redshifted with respect to the centroid

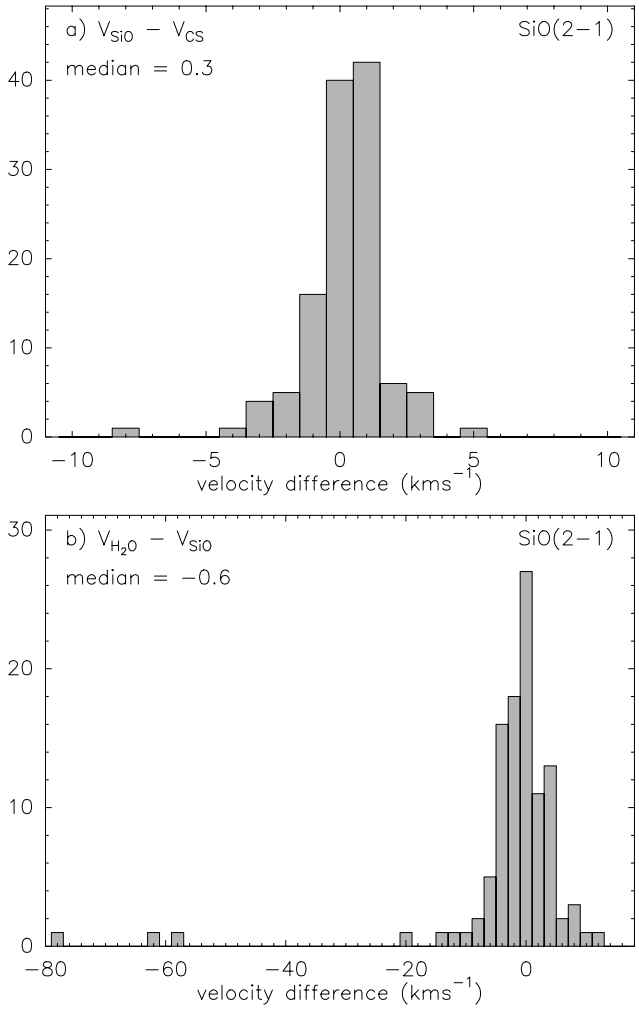

Fig. 9. The distribution of velocity separation of the SiO($J = 2 - 1$) emission peaks with respect to **a)** the CS line peaks and **b)** the H_2O maser line peaks in our sample

are 0.01 ± 0.26 and 0.00 ± 0.28. However, it is evident in the histograms and in the spectral figures of the Appendix B, that there is a number of highly asymmetric profiles with a steep rise on one side of the peak and a gradual fall on the other. The significance of full widths and the degree of asymmetry of the lines for the shock models are discussed in Sect. 5.4.

4.3. Peak velocities

For most sources detected in SiO, the velocities of the associated dense molecular cores as estimated from CS data are available. For this purpose we have used the surveys of Plume et al. (1992, 1997), Bronfmann et al. (1996), Juvela (1996) and Zinchenko et al. (1994, 1995). The distribution of the velocity differences between the SiO($J = 2 - 1$) line peaks and the CS line peak are shown in Fig. 9a. Figure 9b represents the corresponding separation with respect to the H_2O maser emission peaks. Both SEST and Onsala data are included. The median velocity differences are indicated in the figure.

The SiO peak velocity is always close to the CS peak and thus the ambient cloud velocity. The average velocity separation (i.e. the absolute value of the difference) between the peaks, and its standard deviation are 1.02 and 1.06, respectively. The largest differences are towards the Onsala sources No. 150 (Jenness 21078 + 5211, -7.2 km s^{-1}) and No. 162 (S140, +4.6 km s^{-1}).

The median SiO−H_2O velocity difference is -0.6 km s^{-1}. This is in consistence with the result of Wouterloot et al. (1995), where a mean separation of -0.6 ± 0.1 km s^{-}1 was found between H_2O and CO line peak velocities for a much larger sample. The scatter in the SiO−H_2O velocity difference is, however, markedly larger than for the pair SiO−CS. The *average* velocity separation between the H_2O and SiO peaks and

its standard deviation are 5.2 and 11.1, respectively. This reflects the fact that H_2O maser components may have large velocities with respect to the ambient cloud. Three maser sources are highly blueshifted with respect to SiO. These objects are IRAS 09002−4412 (SEST No. 32, velocity difference -56 km s^{-1}), NGC 6334 or GGD25 (SEST No. 131, -78 km s^{-1}) and W51N (Onsala No. 104, -58 km s^{-1}).

4.4. Line ratios

According to the shock chemistry model and SiO profile computations performed by Schilke et al. (1997), the integrated intensity ratio $J = 3-2/J = 2-1$ depends on the pre-shock density. As indicated in their Fig. 6, the $J = 2-1$ line is stronger than $J = 3-2$ at low densities but weaker at high densities. The intensities are roughly equal at $n_{\rm H} = 10^5$ cm^{-3}.

The distribution of the integrated antenna temperature $J = 3{-}2/J = 2{-}1$ in our SEST observations is shown in Fig. 10. The median of the distribution is 1.1. The antenna temperature ratio can be converted to the brightness temperature ratio taking the different beam sizes and beam efficiences at the transition frequencies into account. The formula needed for this conversion is given in Anglada et al. (1996), Eq. (A2). The antenna and beam efficiencies and beam widths for the SEST are given in Table 1. For a circular source with uniform surface brightness, the conversion factor between the $T_{\rm B}(3-2)/T_{\rm B}(2-1)$ ratio and the corresponding $T_{\rm A}^*$ ratio ranges from 0.54 (for very small sources) to 1.1 (for extended sources). If the source size is smaller than $1'$ the conversion factor is less than 0.75. According to the existing SiO maps sources are typically small and the conversion factor is probably close to the lower limit 0.54. In the light of the calculations of Schilke et al. (1997) the observed $J = 3-2/J = 2-1$ ratios suggest that the typical gas densities in the studied regions are moderate ($\leq 10^5$ cm^{-3}).

Without maps and observations of rare isotopomers this cannot confirmed, however. In LTE the brightness temperature ratio $T_{\rm B}(3-2)/T_{\rm B}(2-1)$ approaches 2.25 at high values of $T_{\rm ex}$ in the optically thin case (see the next subsection). This is the absolute maximum since the ratio decreases along with the optical thickness and approaches unity at very high values of the SiO column density. The integrated intensity ratios are likely to follow the optically thin case even though the optical thickness is probably high at the line peaks. Depending on the source sizes the few cases with $J = 3-2/J = 2-1$ ratios close to 2 may represent high values of $T_{\rm ex}$ and thus high densities.

4.5. Excitation temperatures

In order to estimate the excitation temperatures of the SiO lines, we measured with SEST the $J = 2-1$ and $J = 3-2$ transitions of both ^{28}SiO and ^{29}SiO towards three strong sources. These are Ori KL (No. 3 in Table B.1.), OH328.81 + 0.63 (No. 91) and G351.77 − 0.54 (No. 135). The obtained spectra are shown in Fig. 11.

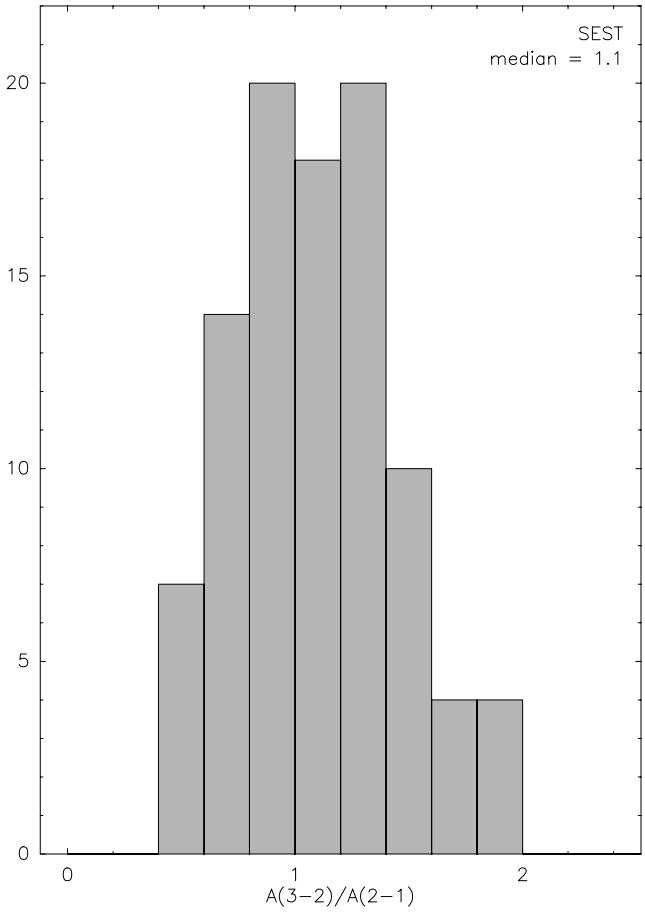

Fig. 10. The integrated intensity ratio of the SiO ($J = 3-2$) and ($J = 2-1$) lines

The $v = 0, J = 2-1$ transition in Ori KL is masing, which is clearly visible in the ^{29}SiO spectrum. The maser components, arising either from an expanding shell (see e.g. Chandler & De Pree 1995) or a rotating disk (Plambeck et al. 1990) around IRc2, are naturally present also in the normal isotope spectrum, but buried in the thermal emission. The maser components of the ^{28}SiO($J = 2-1$) spectrum can be traced by dividing the purely thermal ^{28}SiO($J = 3-2$) spectrum by the former, which brings out two deep dips at the same velocities where also the ^{29}SiO peaks are located. This is caused by the fact that the brightness temperature ratio SiO($J = 2-1$)/($J = 3-2$) lines increases sharply at velocities corresponding to the regions where the population inversion between the levels $J = 2$ and $J = 1$ occurs. The $v = 0$ maser components are at -6.8 and 16.2 km s^{-1} i.e. at slightly larger offsets from the molecular cloud velocity than the $v = 1$ features.

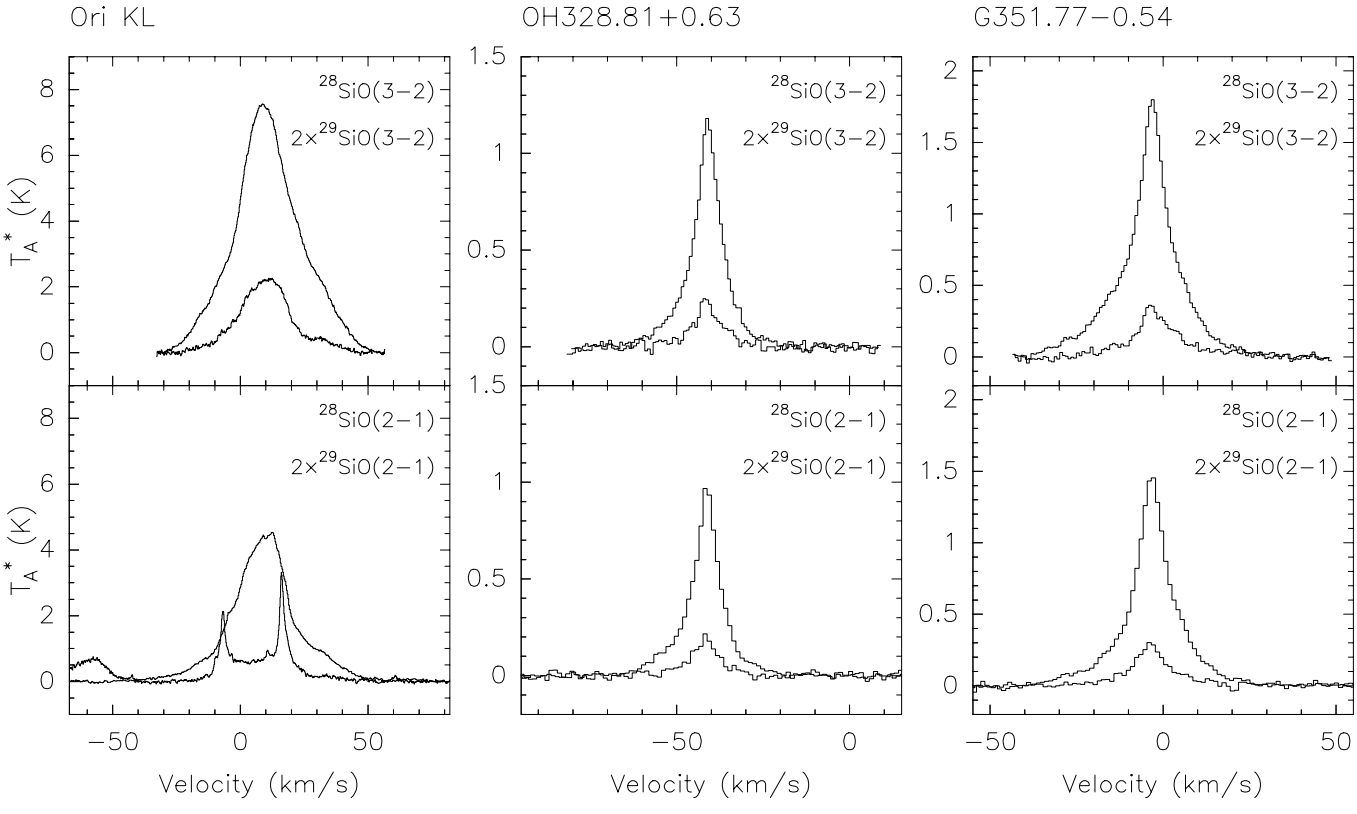

Fig. 11. The $v = 0, J = 3-2$ and $v = 0, J = 2-1$ lines of ^{28}SiO and ^{29}SiO towards Ori KL, OH328.81 + 0.63 and G351.77 − 0.54. The weaker ^{29}SiO spectra are multiplied by 2

In LTE the optical thickness ratio of the transitions $3 \rightarrow 2$ and $2 \rightarrow 1$, as a function of the excitation temperature $T_{\rm ex}$, is approximately

$$\frac{\tau_{3\rightarrow2}}{\tau_{2\rightarrow1}} \approx \frac{3}{2} \mathrm{e}^{-3E_1/T_{\rm ex}} \frac{\mathrm{e}^{3E_1/T_{\rm ex}} - 1}{\mathrm{e}^{2E_1/T_{\rm ex}} - 1}, \quad (2)$$

where $E_1 \equiv h\nu_{10}/k$ equals 2.08 K for the SiO molecule in the vibrational ground state. The optical thickness ratio $\tau(3-2)/\tau(2-1)$ for SiO exceeds unity when $T_{\rm ex}$ is greater than about 7 K, and the upper limit of the ratio when $T_{\rm ex}$ approaches infinity is $(3/2)^2 = 2.25$. The ratios at the line peaks for Ori KL, OH328.81 + 0.63 and G351.77 − 0.54 are 1.6, 0.9 and 1.0, respectively. The corresponding values of $T_{\rm ex}$ from the LTE assumption are 18, 6 and 7 K.

For the thermal sources the optical thickness ratios do not change considerably over the velocity ranges where the signal to noise ratio is reasonable, i.e. $-55 \rightarrow -35$ km s^{-1} and $-15 \rightarrow 10$ km s^{-1} for OH328.81 + 0.63 and G351.77 − 0.54, respectively, suggesting that the excitation temperatures are equally low in the high-velocity gas.

The derived excitation temperature (18 K) towards Ori KL is much lower than the kinetic temperature of the SiO emission region ($\sim$ 200 K, see. e.g. Deguchi & Nguyen-Quang-Rieu 1983). The derived excitation temperatures (6 and 7 K) are very likely to be lower than the kinetic temperatures also in the two other sources.

Acord et al. (1997) derived, from NH_3 and CO observations, a kinetic temparature of 100 K for the outflowing gas associated with the ultracompact HII region and outflow source G5.89-0.39 (close to the H_2O maser W28 A2(2), No. 144 in Table B.2). They also observed several SiO transitions towards this source and used statistical equilibrium calculations for determining other physical parameters of the outflowing gas. The rotational temperature of SiO was found to be about 12 K, i.e. clearly subthermal.

The low values of $T_{\rm ex}$ derived for the mentioned four sources suggest that the average densities of the SiO emission regions there are not particularly high. They probably remain below the critical density of the SiO($v = 0, J = 3-2$) line, $\sim 3\,10^6$ cm^{-3} at 100 K (Turner et al. 1992), and are thus clearly lower than the densities required for H_2O maser excitation, i.e. $n_{\rm H_2} \sim 10^9$ cm^{-3}.

5. Bow-shock models

We have calculated spectral line profiles expected from three bow-shock models:

1) bow shocks generated by a high-velocity jet impacting on the ambient medium according to the model of Hartigan et al. (1987) with the modification made by Dutrey et al. (1997);

2) bow shocks surrounding UC HII regions generated by the movement of the central star through the ambient medium according to the analytical model of Wilkin (1996); and

3) turbulent wakes behind bow shocks in protostellar jets according to the model of Raga & Cabrit (1993).

It is assumed that the bow-shock is unresolved by the telescope beam. The calculations performed here are qualitative and merely used to test whether any of these models could be utilized in a more detailed analysis of the SiO profiles. The lines are assumed to be optically thin. In models 1) and 2) the shocked gas is furthermore assumed to be isothermal.

In Fig. 12 spectra from an approximate analysis are shown. In all the models the basic form of the spectrum depends strongly on the viewing angle ϕ, which is defined as the angle between the symmetry axis of the bow (going through its apex) and the line of sight (see Fig. 1 in Hartigan et al. 1987). $\phi = 0$ means the situation where the apex is pointing towards the observer. The velocity is expressed in terms of the shock ($v_{\rm s}$), central star ($v_\star$) or jet velocity ($v_{\rm j}$) in models 1, 2 and 3, respectively. The parameter $\sigma_{\rm v}$ is the chaotic velocity dispersion in the mentioned units.

Provided that the density and temperature distributions are not sharply peaked towards the apex, the emission line profile from a bow-shock is dominated by the 'tail' since the apex occupies a relatively small volume. In all models discussed here high velocities occur close to the apex whereas the velocity in the tail approaches the ambient velocity. Therefore the velocity of the peak intensity is always close to the ambient cloud velocity, whereas the "wings" are seen at high velocities. The adopted models are described in some detail in Appendix A.

5.1. Comparison with the observed profiles

In a comparison between the obtained SiO profiles and the predictions of the kinematical bow shock models the following observational facts are noteworthy:

1) the peak intensities appear always close to the ambient cloud velocity;

2) the full widths above two sigma of the SiO lines are between 2 and 60 km s^{-1}, except for Ori KL with a *FW* of about 100 km s^{-1};

3) the main isotope SiO lines never exhibit double peaked profiles.

The fact that the SiO lines always peak close to the ambient cloud velocity implies that the emission does not come from plane parallel shocks or from shocked cloudlets exposed to stellar wind or jets. Both in a planar shock and in a shocked cloudlet the intensity maxima occur at the projected shock velocity (see Schilke et al. 1997), and probably we sometimes would see such a shock "face-on" (i.e. at a small viewing angle), causing the SiO emission peak to be clearly shifted with respect to the ambient gas. Therefore models where a jet or the exciting star itself, when penetrating through the cloud, accelerates a small portion of gas to high velocities, are more plausible. In terms of the Hartigan-Dutrey model (1) this observation means that the ambient gas is not considerably pre-accelerated i.e. the parameter γ is small.

In models 1 and 2 the full width above zero intensity (FWZI) of the line is roughly equal to the jet or stellar velocity, irrespective of the viewing angle ϕ. The absolute line widths in model 2 should be markedly smaller than in model 1. The velocity of a star with respect to the ambient cloud is of the order of 10 km s^{-1} (Churchwell 1991), whereas jet velocities can be as high as $100 - 300$ km s^{-1}. The distribution of full widths above two sigma (Fig. 7) clearly indicates that a major part of the SiO emission regions are associated with high velocity outflows driven by jets. It is likely that in some cases the observed SiO profile is a result of the superposition of several jet working surfaces or UC HII regions. The cases where both blue- and redshifted linewings are present may represent bipolar distribution, which together with successive jet acceleration (Dutrey et al. 1997) provides an explanation for very large velocity dispersions.

The large variation in the full widths and absence of thermal double peaked profiles suggest that bow-shocks (models 1 and 2) do not provide a universal model for the SiO emission. Otherwise one would expect that the full widhts are always 10 km s^{-1} or more, and that at least in some cases we see the shock edge-on causing the observed profile to be double peaked.

In contrast, the triangular line shapes and changing line widths predicted by the turbulent wake model of Raga & Cabrit (1993) fit the observed profiles rather well. However, the observed distribution of the asymmetry parameter P (Fig. 8) is not what one would expect by assuming an isotropic orientation of wakes. In the model of Raga & Cabrit the asymmetry parameter P as a function of the viewing angle ϕ is simply $-\cos\phi$. In reality the extreme velocities would not be detected due to noise in the spectra, and the cosine function would be "flattened" i.e. $|P|$ would never reach the value 1. Nevertheless, in a histogram like the one presented in Fig. 8 the largest number of sources should occur in the range where $P(\phi)$ changes least i.e. close to the *extrema*, and the pattern should be double peaked which apparently is not the case. Similarly, the normalized peak position (NPP) for the H_2O maser sample of Wouterloot et al. (1995, see their Fig. 3) never shows a two-peaked distribution. This was in contradiction with the earlier results of Palagi et al. (1993), and lead Wouterloot et al. to the conclusion that NPP is not useful to characterize the emission. The fact that maser emission

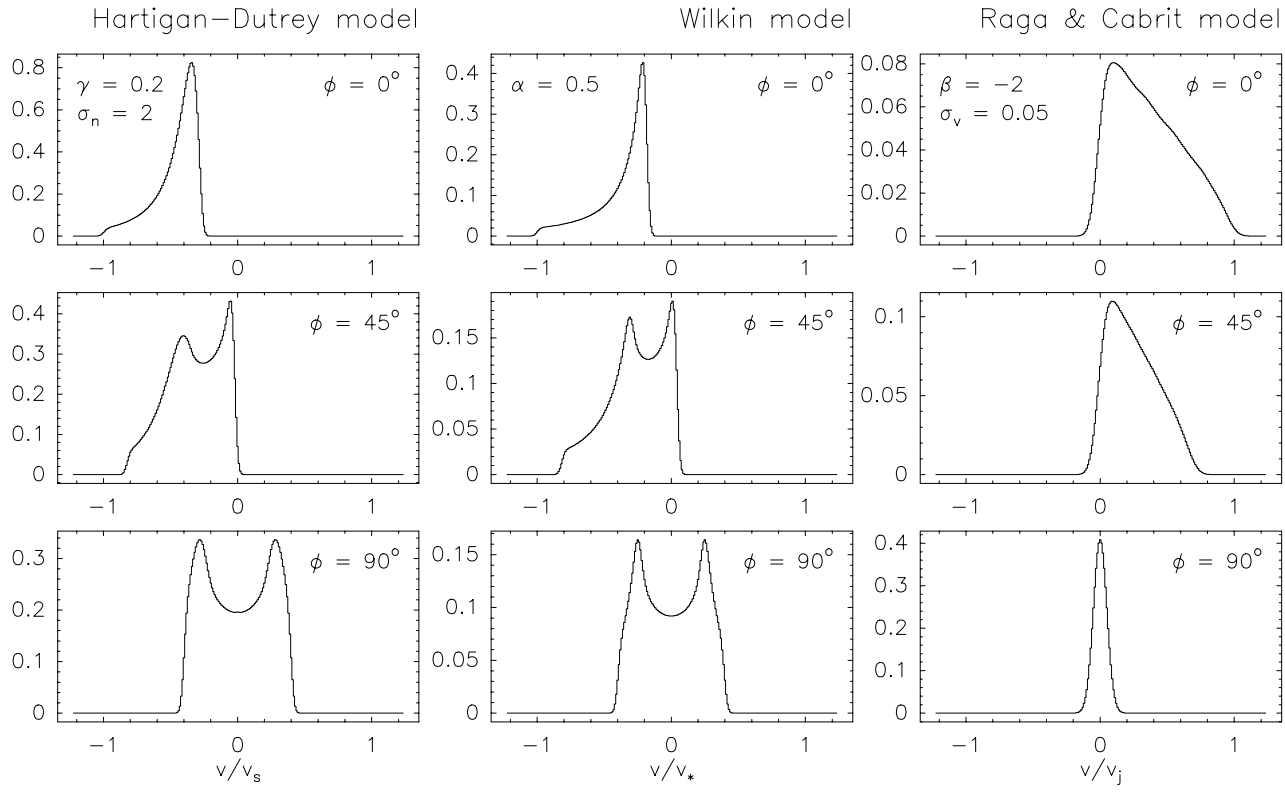

Fig. 12. Simulated spectra from a bow-shock according to the models (1), (2) and (3) (see text) with different viewing angles. Inclination 0° means the case where the shock is seen "head on", and 90° means the "edge on" case. The angular size of the object is assumed to be smaller than the telescope beam size. The velocity has been expressed in units of the shock velocity (v_s, model 1), stellar velocity ($v_\star$, model 2) or jet velocity (v_j, model 3). σ_v is the turbulent velocity dispersion. The meaning of the other parameters can be found in the referred papers and Appendix A

is known to often arise from separate spots makes the difficulty of its characterization understandable. Presumably the situation with thermal SiO emission is less complex. However, if the emission does not come from a single region the asymmetry parameter fails to describe the orientation of the shock. For example if the source is bi-polar but unresolved $P(\phi)$ is always 0.

The determination of the expected full width distribution in the model of Raga & Cabrit is difficult since the jet velocity v_j probably changes from source to source. The full width is approximately $\Delta v_{\rm turb} + v_j\,|\cos\phi|$ and, on the basis of similar arguments as in the case of P, values of the full width which are close to v_j should occur more frequently. One would expect the FW distribution to be peaked towards larger values since the jet velocities are likely to be at least a few times 10 km s^{-1}.

Taken the relatively large number of narrow SiO lines it is doubtful if one can reproduce both P- and FW-distributions at the same time with the aid of Raga & Cabrit model, even by combining mono- and bipolar sources. Therefore it seems likely that at least in some sources SiO emission arises from the quiescent gas component, due to processes discussed in the next section.

6. Discussion

The SiO detection rate is the highest towards those H_2O masers and UC HII regions which are associated with IRAS sources having large integrated FIR flux densities and luminosities. Since SiO emission is indicative of the presence of shocks, this tendency might be understood in terms of the correlation discovered by Felli et al. (1992), between the mechanical luminosities of outflows associated with H_2O masers and IRAS source FIR luminosities.

On the other hand, the detection rate was found to be higher in the galactic longitude range $300° \leq l < 60°$ than elsewhere. By limiting the sample to objects which are associated with luminous IRAS point sources, it was shown that the higher detection rate in this part of the sky is not caused barely by the fact that the selected sources there are associated with FIR sources brighter than the

average. Most sources in this longitude range are located between the galactocentric radii 3 and 7 kpc, which region is sometimes referred to as the "molecular ring". It seems therefore possible that the conditions of the dense molecular cores in the inner 7 kpc of the Galaxy, where most of the massive star formation is taking place, are particularly favourable for gas-phase SiO production.

According to Schilke et al. (1997) shock velocities in excess of 10 km s^{-1} are needed for grain mantle evaporation, whereas the silicate cores are destroyed at velocities greater than about 25 km s^{-1}. The majority of the SiO lines detected in the present survey have full-widths greater than 10 km s^{-1} indicating that high-velocity shocks indeed are an important production channel for SiO also in high-mass star forming regions. The line shapes suggest that SiO emission at large velocities arise from turbulent wakes behind bow-shocks, i.e. post-shock gas. The derived excitation temperatures of the SiO transitions and the $(3-2)/(2-1)$ line ratios suggest moderate average densities, supporting the notion of filled-in cavities. In this gas component SiO is probably rather short-lived due to further oxidation to SiO_2 (Schilke et al. 1997). Therefore high-velocity SiO emission is a sign of recent outflow activity.

Several of our target sources have been observed with the IRAM 30-m telescope in the transitions $J = 2-1$, $J = 3-2$ and $J = 5-4$ of SiO by Acord et al. (1998). A comparison between the results shows that while the integrated line intensities and the FWHMs of the lines are comparable, the full widths observed at IRAM are systematically larger than those observed at SEST and Onsala. This is probably due to a combination of two effects. Firstly, high velocity emission regions are likely to be compact and better traced with the 30-m telescope, which has an effective aperture 3.4 times larger than the SEST at 3 mm. Second, in a quick survey like the present the spectral noise cuts the lowest intensity line wings.

As pointed out by Acord et al. (1998), due to the fact that the mass distribution as a function of velocity, $m(v)$, approximately follows the power law $m(v) \propto v^{-\gamma}$, where γ is close to 2 (Masson & Chernin 1992, 1994), the spectra of outflow sources often bear a resemblance of Lorentzian profiles characteristic of pressure broadening. In the latter case the observed full width depends heavily on the intensity threshold where it is determined. This arouses the suspicion that the distribution of FWs (full widths above two sigma) in Fig. 7 does not reflect true changes in the velocity extent of the SiO lines, but is determined by the S/N ratios. We have examined the dependence of the full widths on the S/N ratio in Fig. 13, where the ratios $FW/\Delta v_{1/2}$ vs. $T_{\rm A}^{\rm peak}/T_{\rm A}^{\rm min}$ for the SiO$(J = 2-1)$ lines are plotted. $\Delta v_{1/2}$ is the FWHM of the line, $T_{\rm A}^{\rm peak}$ is the peak antenna temperature and $T_{\rm A}^{\rm min}$ is the intensity threshold used for estimating the FW. The ratio $T_{\rm A}^{\rm peak}/T_{\rm A}^{\rm min}$ represents here the S/N ratio of the smoothed spectra. For a Gaussian profile,

$$\frac{T_{\rm A}^{\rm peak}}{T_{\rm A}^{\rm min}} = \exp\left\{\ln 2 \left(\frac{FW}{\Delta v_{1/2}}\right)^2\right\} .$$

The ratio $FW/\Delta v_{1/2}$ is thus proportional to the square root of the logarithm of the S/N ratio. The relation expected from Gaussian line shapes is plotted as a dotted curve in Fig. 8. For the sake of comparison we have also plotted the expected relation for Lorentzian shapes as a dashed curve. For the latter

$$\frac{T_A^{\rm peak}}{T_A^{\rm min}} = 1 + \left(\frac{FW}{\Delta v_{1/2}}\right)^2 ,$$

and the ratio $FW/\Delta v_{1/2}$ is roughly proportional to the square root the S/N ratio. In Fig. 13 it can be seen that several spectra follow the Gaussian curve which slopes only gently beyond a S/N ratio of about 10. In these cases the determined full widths give reasonable estimates of the FWZIs (full widths at zero intensity). On the other hand, the observations above the Lorentzian curve have relatively low S/N ratios, and probably a longer integration would have revealed extensive line wings. Nevertheless, Fig. 13 bears evidence of intrinsically narrow lines and confirms that the histogram in Fig. 2 depicts underlying changes of the FWZIs for the emission regions covered by the SEST beam.

The detection of narrow, Gaussian SiO lines and the fact that none of the discussed kinematical models can satisfactorily explain the observed distribution of the line profiles make it plausible, however, that the observed lines have a substantial contribution from quiescent gas, where

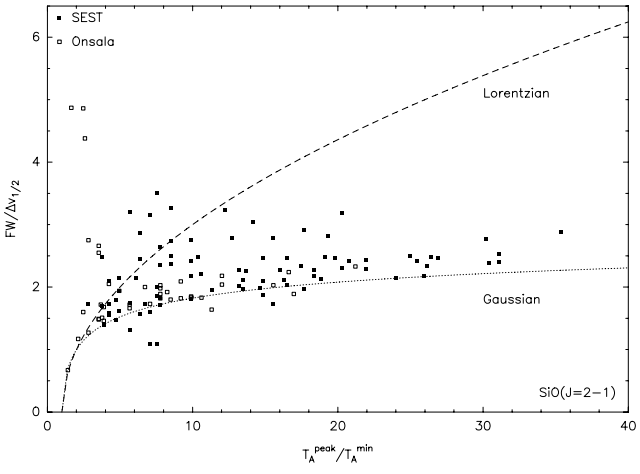

Fig. 13. The ratio $FW/\Delta v_{1/2}$ as a function of $T_{\rm A}^{\rm peak}/T_{\rm A}^{\rm min}$ for the SiO$(J = 2-1)$ lines detected with SEST (filled squares) and Onsala (open squares). $T_{\rm A}^{\rm min}$ is the intensity threshold used for the determination of FW (see text), and $T_{\rm A}^{\rm peak}/T_{\rm A}^{\rm min}$ thus represents the S/N ratio. The dotted curve represents the expected relation in the case of a Gaussian line shape and the dashed curve represents a Lorentzian

SiO production has not occured by means of high-velocity outflows. In the chemistry model of McKay (1995, 1996) the main reservoir of Si in grain mantles is SiH_4, which can evaporate into the gas phase in warm conditions. To form SiO, SiH_4 needs first to be deprived of the hydrogen atoms, which can take place through reactions with neutral hydrogen or, with a much higher efficiency, with ionized carbon C^+ (McKay 1996).

Enhanced abundances of C^+ and other ions required to speed up the formation of SiO can be the result of the X-ray, EUV, and FUV radiation from shocks. According to the model of Wolfire & Königl (1993) high-energy photons from shocks can cause an overabundance of ions and produce electronic heating in ambient dense clumps. In this way they explain the enhanced HCO^+ emission *ahead* the shock fronts observed towards several Herbig-Haro objects. Another possible source of energetic radiation in star-forming regions is the magnetic field activity close to the protostellar surface (Montmerle et al. 1993).

The high SiO detection rate between the galactocentric radii 3 and 7 kpc for a luminosity limited sample can be due to some additional mechanism apart from protostellar shocks which sustain elevated temperatures also in the relatively quiescent dense gas in the "molecular ring". There are several alternativies. Cloud-cloud collisions and shocking by the spiral density waves are supposed to be particularly effective in the inner Galaxy (e.g. Sakamoto et al. 1997). The heating might be also caused by increased interstellar radiation field or by embedded OB stars (Bronfman 1992 and references therein).

SiO emission may originate from regions with very different characteristics: 1) dense gas heated by the radiation from a bow-shock (Wolfire & Königl 1993) or by some of the "external" mechanism mentioned above; and 2) post-shock gas filling the cavity behind the bow-shock (Raga & Cabrit 1993). Does SiO then serve our original purpose i.e. the study of shock fronts associated with maser emission? We think so since firstly, with the aid of models like that of Raga & Cabrit (1993) "shocked" profiles can be used for estimating the jet velocity and thereby the momentum input to the ambient gas. Second, with the aid of narrow SiO emission features detected towards some sources the dense gas ahead of shock fronts can be traced. It is clear, however that observations of higher J-transitions combined with model calculations like those performed by Schilke et al. (1997) are required for determining the physical characteristics of the densest regions providing favourable environment for maser excitation.

7. Conclusions

We have detected a large number of new thermal SiO sources in the regions of massive star formation. Most detections are made towards strong H_2O masers. Further investigation showed that the detection rate is the highest towards objects associated with IRAS sources with large FIR luminosities. This is probably related to the earlier results that the FIR luminosity correlates with the maximum H_2O luminosity (Wouterloot et al. 1995), and that the mechanical luminosity of outflow associated with H_2O masers correlates with the maser luminosity (Felli et al. 1992). Although more subtle mechanisms have been suggested, the fact that powerful shocks are required for both destruction of silicate grains and the most commonly accepted pumping mechanism of H_2O masers, makes these relations understandable. Since FIR emission comes from circumstellar dust heated by the radiation from the central star, its correlation with the SiO detection rate suggests that the occurrence of shocks depends on the stellar luminosity.

A FIR luminosity limited sample of IRAS sources revealed also a spatial dependence in the SiO detection rate. For sources with $\log L_{\rm FIR}/L_\odot > 4$ the detection rate in the galactic longitude range $300^\circ \leq l < 60^\circ$ is roughly twice as high as in the other two equal intervals of longitude. About 90% of the sources in the mentioned longitude range are located between the galactocentric radii 3 and 7 kpc.

The full widths above two sigma of the SiO lines vary from 2 to 103 km s^{-1} and they always have a single peak. The latter characteristic implies that bow-shocks do not provide a generally applicable model for the SiO emission regions. A better agreement with the observations is obtained by the model of turbulent wakes *behind* bow-shocks by Raga & Cabrit (1993), where the FWZI and the line asymmetry depends on the viewing angle. However, the number of narrow and symmetric line profiles suggests that the SiO formation also takes place in relatively quiescent gas, perhaps due to grain mantle evaporation and subsequent chemical processing aided by ionizing radiation from shocks. The higher detection rate in the inner 7 kpc of the Galaxy may be partly due to the latter processes. It is possible that in this region, where the molecular gas surface density is large and the star formation rate is high (e.g. Blitz 1997; Bronfman 1992), the dense cores are warmer and have higher column or volume densities, and thereby provide appropriate conditions for the production and excitation of SiO.

The data provide a basis for further investigation of shocks associated with massive young stars. In a subsequent paper we shall study the velocities of H_2O, OH and CH_3OH masers with respect to the observed SiO line profiles, utilizing the existing interferometric maps of the spatial distribution of masers and UC HII regions.

The excitation temperatures derived from the SiO data towards three sources are subthermal and do not show variation in velocity ranges of about 20 km s^{-1}. This agrees with the results of Acord et al. (1997) towards the massive outflow source G5.89−0.39 and indicates that the determination of kinetic temperature of shocked gas is not possible with the aid of two transitions of SiO only.

Acknowledgements. We thank the referee, Dr. J. Brand, for a careful reading of the manuscript and for very helpful comments and suggestions. We are grateful to him and Dr. J.G.A. Wouterloot for the program for calculating kinematic distances. We thank also Dr. C.M. Walmsley and Prof. K. Mattila for useful information and discussions. This work by J.H. and K.L. has been supported by the Finnish Academy through grant No. 1011055. The Swedish-ESO Submillimetre Telescope is operated jointly by ESO and the Swedish National Facility for Radio Astronomy, Onsala Space Observatory at Chalmers University of Technology.

References

Acord J.M., Walmsley C.M., Churchwell E., 1997, ApJ 475, 693
Acord J.M., Walmsley C.M., Churchwell E., 1998, ApJ (submitted)
Anglada G., Estalella R., Pastor J., Rodríguez L.F., Hashick A.D., 1996, ApJ 463, 205
Avedisova V.S., Palouš J., 1989, Bull. Astron. Inst. Czechosl. 40, 42
Bachiller R., 1996, ARA&A 34, 111
Blitz L., 1997, in CO: Twenty-Five Years of Millimeter-Wave Spectroscopy, Latter W.B., Radford S.J.E., Jewell P.R., Magnum J.G., Bally J. (eds.). Kluwer Academic Publishers, Dordrecht, p. 11
Booth R.S., Delgado G., Hagström M., et al., 1989, A&A 216, 315
Brand J., 1986, Ph.D. thesis, University of Leiden
Brand J., Blitz L., 1993, A&A 275, 67
Brand J., Cesaroni R., Caselli P., et al., 1994, A&AS 103, 541
Braz M.A., Epchtein N., 1983, A&AS 54, 167
Braz M.A., Gregorio Hetem J.C., Scalise E. Jr., Monteiro do Vale J.L., Gaylard M., 1989, A&AS 77, 465
Braz M.A., Lepine J. R.D., Sivagnanam P., Le Squeren A.M., 1990, A&A 236, 479
Bronfman L., 1992, in The Center, Bulge, and Disk of the Milky Way, Blitz L. (ed.). Kluwer Academic Publishers, Dordrecht, p. 131
Bronfman L., Nyman L.-Å., May J., 1996, A&AS 115, 81
Caswell J.L., 1996, MNRAS 279,79
Caswell J.L., 1997, MNRAS 289, 203
Caswell J.L., Haynes R.F., 1983a, Aust. J. Phys. 36, 361-399
Caswell J.L., Haynes R.F., 1983b, Aust. J. Phys. 36, 417-442
Caswell J.L., Vaile R.A., 1995, MNRAS 273, 328
Caswell J.L., Batchelor R.A., Forster J.R., Wellington K.J., 1983a, Aust. J. Phys. 36, 401-415
Caswell J.L., Batchelor R.A., Forster J.R., Wellington K.J., 1983b, Aust. J. Phys. 36, 443-451
Caswell J.L., Vaile R.A., Forster J.R., 1995, MNRAS 277, 210
Cernicharo J., Bachiller R., Duvert G., 1985, A&A 149, 273
Cesaroni R., 1990, A&A 233, 513
Cesaroni R., Walmsley C.M., Kömpe C., Churchwell E., 1991, A&A 252, 278
Chan S.J., Henning T., Schreyer K., 1996, A&AS 115, 285
Chandler C.J., De Pree C.G., 1995, ApJ 455, L67
Churchwell E., 1991, in The Physics of Star Formation and Early Stellar Evolution, Lada C.J., Kylafis N.D. (eds.). Kluwer Academic Publishers, p. 221
Churchwell E., Walmsley C.M., Cesaroni R., 1990, A&AS 83, 119
Clemens D.P., Barvainis R., 1988, ApJS 68, 257
Codella C., Felli M., 1995, A&A 302, 521
Comoretto G., Palagi F., Cesaroni R., et al., 1990, A&AS 84, 179
Dame T.M., Ungerechts H., Cohen R.S., et al., 1987, ApJ 322, 706
Deguchi S., Nguyen-Quang-Rieu, 1983, A&A 117, 314
Downes D., Genzel R., Hjalmarson Å., Nyman L.-Å., Rönnäng B., 1982, ApJ 252, L29
Dutrey A., Guilloteau S., Bachiller R., 1997, A&A 325, 758
Elitzur M., Hollenbach D.J., McKee C.F., 1989, ApJ 346, 983
Ellingsen S.P., von Bibra M.L., McCulloch P.M., et al., 1996, MNRAS 280, 378
Emerson J.P., 1988, in Duprée A.K., Lago M.T.V.T. (eds.) Formation and Evolution of Low Mass Stars, Kluwer, p. 193
Felli M., Palagi F., Tofani G., 1992, A&A 255, 293
Fich M., Blitz L., Stark A.A., 1989, ApJ 342, 272
Forster J.R., Caswell J.L., 1989, A&A 213, 339
Forster J.R., Caswell J.L., Okumura S.K., Hasegawa T., Ishiguro M., 1990, A&A 231, 473
Gardner F.F., Whiteoak J.B., 1978, MNRAS 183, 711
Gaume R.A., Mutel R.L., 1987, ApJS 65, 193
Gensheimer P.D., Mauersberger R., Wilson T.L., 1996, A&A 314, 281
Genzel R., Downes D., 1977, A&AS 30, 145
Georgelin Y.M., Georgelin Y.P., 1976, A&A 49, 57
Hartigan P., Raymond J., Hartmann L., 1987, ApJ 316, 323
Haschick A.D., Moran J.M., Rodríguez L.F., Ho P.T.P., 1983, ApJ 265, 281
Henning T., Cesaroni R., Walmsley C.M., Churchwell E., 1992, A&AS 93, 525
Henning T., Pfau W., Altenhoff W.J., 1990, A&A 227, 542
Hofner P., Churchwell E., 1996, A&AS 120, 283
Jenness T., Scott P.F., Padman R., 1995, MNRAS 276, 1024
Jenniskens P., Wouterloot J.G.A., 1990, A&A 227, 553
Joncas G., Durand D., Roger R.S., 1992, ApJ 387, 591
Juvela M., 1996, A&AS 118, 191
Lada E.A., Bally J., Stark A.A., 1991, ApJ 368, 432
Martín-Pintado J., Bachiller R., Fuente A., 1992, A&A 254, 315
Masson C.R., Chernin L.M., 1992, ApJ 387, L47
Masson C.R., Chernin L.M., 1994, in Clouds, Cores and Low Mass Stars, ASP Conf. Ser. 65, Clemens D.P., Barvainis R. (eds.) p. 350
McKay D.D.S., 1995, MNRAS 274, 694
McKay D.D.S., 1996, MNRAS 278, 62
Menten K.M., 1991, ApJ 380, L75
Menten K.M., Reid M.J., Pratap P., Moran J.M., Wilson T.L., 1992, ApJ 401, L39
Molinari S., Brand J., Cesaroni R., Palla F., 1996, A&A 308, 573
Montmerle T., Feigelson E.D., Bouvier J., André P., 1993, in Protostars and Planets III, Levy E.H. & Lunine J.I. (eds.). The University of Arizona Press, p. 689
Moreira M.C., Yun J.L., 1995, ApJ 454, 850
Palagi F., Cesaroni R., Comoretto G., Felli M., Natale V., 1993, A&AS 101, 153
Plambeck R.L. Wright M.C.H., Carlström J.E., 1990, ApJ 348, L65

Plume R., Jaffe D.T., Evans N.J. II, 1992, ApJS 78, 505
Plume R., Jaffe D.T., Evans II N.J., Martín-Pintado J., Gómez-González J., 1997, ApJ 476, 730
Raga A., Cabrit S., 1993, A&A 278, 267
Sakamoto S., Hasegawa T., Handa T., Hayashi M., Oka T., 1997, ApJ 486, 276
Scalise E. Jr., Rodríguez L.F., Mendoza-Torres E., 1989, A&A 221, 105
Schilke P., Walmsley C.M., Pineau des Fôrets, Flower D.R., 1997, A&A 321, 293
Simpson J.P., Rubin R.H., 1990, ApJ 354, 165
Turner B.E., Chan K.-W., Green S., Lubowich D.A., 1992, ApJ 399, 114
Van Buren D., Mac Low M.-M., Wood D.O.S., Churchwell E., 1990, ApJ 353, 570
van der Walt D.J., Gaylard M.J., MacLeod G.C., 1995, A&AS 110, 81
Wilkin F.P., 1996, ApJ 459, L31
Wolfire M.G., Königl A., 1993, ApJ 415, 204
Wood D.O.S., Churchwell E., 1989, ApJ 340, 265
Wouterloot J.G.A., Brand J., 1989, A&AS 80, 149
Wouterloot J.G.A., Walmsley C.M., 1986, A&A 168, 237
Wouterloot J.G.A., Walmsley C.M., Henkel C., 1988, A&A 203, 367
Wouterloot J.G.A., Fiegle K., Brand J., Winnewisser G., 1995, A&A 301, 236
Xiang D., Turner B.E., 1995, ApJS 99, 121
Zinchenko I., Forsström V., Lapinov A., Mattila K., 1994, A&A 288, 601
Zinchenko I., Mattila K., Toriseva M., 1995, A&AS 111, 95

Appendix A: Description of the bow-shock models

A.1. Hartigan-Dutrey model

In model 1 the bow shock shape is simply assumed to be parabolic, i.e. that the constant B in Eq. (1) in Dutrey et al. (1997) is zero. Dutrey et al. (1997) assumed that the ambient material consists of a low-velocity molecular outflow. The ratio of the ambient and shock velocities ($V_{\rm amb}/V_{\rm shock}$) is described by the parameter γ, which in the example spectrum is set to 0.2. This situation represents the case where the ambient medium into which the jet is penetrating moves at a relatively low velocity with respect to the exciting source. Accordingly the peak emission is slightly shifted from the ambient cloud velocity at small viewing angles. As in Dutrey et al. (1997) the density distribution is supposed to be gaussian as a function of the distance from the apex. This distribution is characterized by the density dispersion σ_n. This quantity as well as other quantities which have the dimension of distance are expressed in the units of the parameter p of a parabola (one half of the distance between the focus and the apex). The observed line of sight velocity of a certain element on the surface of the shock (in the units of the shock velocity) is

$$\frac{v_{\rm rad}}{v_{\rm shock}} = (1-\gamma)\frac{\rho}{1+\rho^2}[\rho\cos\phi + \sin\phi\cos\psi] - \cos\phi\,, \quad \text{(A1)}$$

where ρ is the radial distance of the element from the bow-shock axis, chosen as the z-axis, in the units of the parameter p:

$$\rho = \frac{\sqrt{x^2+y^2}}{p}; \quad \frac{z}{p} = \frac{1}{2}\rho^2\,, \quad \text{(A2)}$$

and ψ is its angle from the direction determined be the line of sight and z axes (chosen as the x-axis, see Fig. 1 in Hartigan et al. 1987). The assumed density weighting function w_n is

$$w_n = \mathrm{e}^{-\frac{1}{2\sigma_n^2}\rho^2\left(1+\frac{\rho^2}{4}\right)}\,. \quad \text{(A3)}$$

The spectrum from the assumed material distribution is obtained by summing up the contributions of all surface elements weighted by their area and surface density.

A.2. Wilkin model

In the model of Wilkin (1996) (model 2), analytical formulae for the shape of the bow shock, tangential velocity and surface density are given as functions of the angular distance θ from the apex (Eqs. 9–12). The observed radial velocity for an element in the units of the central star velocity is

$$\frac{v_{\rm rad}}{v_\star} = \frac{1}{c}[a\cos\phi - b\sin\phi\cos\psi] - \cos\phi\,, \quad \text{(A4)}$$

where

$$\begin{aligned} a &= \varpi^2 - \sin^2\theta \\ b &= \theta - \cos\theta\sin\theta \\ c &= 2\alpha(1-\cos\theta) + \varpi^2\,. \end{aligned} \quad \text{(A5)}$$

ϖ is the cylindrical radius in the units of the standoff distance R_0, which is determined by Eq. (1) in Wilkin (1996). The dependence of ϖ on the apex angle θ is given by Eq. (10) in Wilkin (1996). The parameter α is the ratio of the central star velocity to the stellar wind velocity $V_\star/V_{\rm wind}$. The resulting profiles are very similar to those in the Hartigan–Dutrey model in the case when $\gamma = 0$ i.e. when the ambient velocity is zero with respect to the exciting source.

A.3. Raga & Cabrit model

Raga & Cabrit (1993) modeled turbulent wakes behind internal working surfaces of jets and the associated bow shocks. Their purpose was to investigate whether molecular outflows could be interpreted as gas entrained in these wakes. The model is best understood by inspecting their Fig. 1. The parameters of the model are the shape of the wake (determined by the index β and the length to width ratio x_0/r_0), and the ratio M_1 between the jet velocity v_j and the sound speed c_1 in the mixing layer. In the calculation of profiles we have used the set of parameters depicted in Fig. 3b in Raga & Cabrit

(1993), namely $\beta = -2$, $M_1 = 20$ and $x_0/r_0 = 5$. In this model, the systematic velocity toward the jet axis (v_r) is very small compared with the sound speed c_1 in the mixing layer, and is therefore neglected. Consequently, when the wake is seen from the side ($\phi = 90°$) the the observed profile is determined by the turbulent motion in the wake. Raga & Cabrit give the distributions of the velocity along the jet axis ($v_x(x,r)$), the density $n(x,r)$ and temperature $T(x,r)$ in their Eqs. (16), (21) and (22), respectively. The line of sight velocity distribution can be obtained by a multiplication by the cosine of the viewing angle ϕ. According to the assumption of optically thin emission the spectrum has been calculated by adding all volume elements weighted by a function of density n and temperature T. The weighting function used is

$$w = n \frac{\mathrm{e}^{-E_\mathrm{u}/T}}{T}\,, \tag{A6}$$

where E_u is the energy of the upper transition level. This function comes from the local absorption coefficient by assuming thermal equilibrium. A further assumption made here is that the background radiation is negligible in the antenna equation. On the basis of the above determination of the excitation temperatures these assumptions are not justified. However, we feel that for the purpose of obtaining a qualitative picture of the profiles produced by this model, the method of calculation is reasonable.

Table B.1. SEST source catalogue and the observed SiO $J = 2 - 1$ and $J = 3 - 2$ line parameters

Source l, b [°] dist. [kpc]	R.A. Dec. (1950)	Line SiO Cat.	$T_A^\star$ [K] F_{peak} [Jy]	rms [K] [Jy]	V_{peak} [km/s]	V_{min} [km/s]	V_{max} [km/s]	V_{cen} [km/s]	V_{mean} [km/s]	FW [km/s]	Width [km/s]	Area [Kkm/s] S [Jykm/s]	P V_{cloud} [km/s]	Remarks
(1)	(2)	(3)	(4)	(5)	(6)	(7)	(8)	(9)	(10)	(11)	(12)	(13)	(14)	(15)
1	5:30:14.5	2 → 1		0.03										J
IRAS 05302−0537	−5:37:52	3 → 2		0.06										
208.90−20.05 0.5[a]		Arc.	20.6	5.4	7.4	6.9	8.3	7.6		1.4		11.1	8.8[10]	Orion A-west
2	5:32:46.4	2 → 1	0.10	0.02	12.0	10.8	13.2	12.0	11.9 ± 0.9	2.4	1.5 ± 0.1	0.20 ± 0.03	0.0	H
IRAS 05327−0457	−4:57:38	3 → 2	0.07	0.02	11.6	10.8	13.2	12.0	11.7 ± 1.4	2.4	1.1 ± 0.1	0.10 ± 0.04	−0.3	
208.57−19.18 0.5[a]		Arc.	11.8	3.4	10.2	7.4	10.7	9.1		3.3		10.2		S279
3	5:32:47.0	2 → 1	4.32	0.02	11.7	−47.7	55.6	3.9	9.32 ± 0.02	103.3	32.89 ± 0.01	122.6 ± 0.3	0.2	A, G, Gen
Ori KL	−5:24:23	3 → 2	7.49	0.15	8.7	−26.2	49.1	11.4	10.83 ± 0.05	75.3	31.18 ± 0.03	221.1 ± 2.0	−0.1	
208.99−19.38 0.5[a]		Arc.	200900	4	7.5	−10.0	25.0	7.5		35.0		16400	9.0[4]	
4	5:32:58.2	2 → 1		0.03										(A)
OMC 2(2)	−5: 7:36	3 → 2		0.07										
208.75−19.22 0.5[a]		Arc.	44.3	2.9	7.4	7.0	10.9	8.9		3.9		69.8	11.3[4]	
5	5:32:59.8	2 → 1		0.03										P208.82−19.24, A
OMC 2(1)	−5:11:29	3 → 2		0.07										
208.82−19.24 0.5[a]		Arc.	152.7	3.8	7.5	6.6	10.6	8.6		4.0		112.1	12.3[2]	
6	5:33:53.2	2 → 1		0.05										
HH1	−6:46:50													
210.42−19.76 0.5[a]		Arc.		2.9										- IRAS 05338−0647
7	5:37:30.9	2 → 1		0.06										J
IRAS 05375−0731	−7:31:51													
211.56−19.29 0.5[a]		Arc.		3.1									4.8[10]	L1641 S3
8	5:39:13.7	2 → 1	0.12	0.03	10.8	9.6	14.4	12.0	11.0 ± 0.9	4.8	1.5 ± 0.1	0.3 ± 0.1	−0.5	A
NGC 2024	−1:57:30	3 → 2	0.08	0.04	10.6	9.0	11.4	10.2	10.7 ± 1.9	2.4	1.2 ± 0.2	0.1 ± 0.1	0.3	
206.57−16.36 0.5[a]		Arc.	28.1	2.6	10.2	9.8	10.7	10.2		0.9		27.1	10.7[4]	Orion B
9	5:41:18.6	2 → 1	0.11	0.01	7.8	−14.8	13.8	−0.5	2.8 ± 0.2	28.6	16.5 ± 0.2	1.5 ± 0.1	0.6	J
IRAS 05413−0104	−1: 4:17	3 → 2	0.19	0.03	9.2	−14.7	13.9	−0.4	4.1 ± 0.2	28.6	13.1 ± 0.1	2.2 ± 0.2	0.7	
206.01−15.48 0.5[a]		Arc.	39.2	3.5	2.4	2.0	2.8	2.4		0.8		38.1	10.2[13]	L1630
10	5:43:35.9	2 → 1		0.04										
HH19−27	−0: 9:26	3 → 2		0.07									10.0[14]	
205.45−14.55 0.5[a]		Arc.		4.5										
11	5:44:31.3	2 → 1	0.11	0.02	12.0	3.7	19.2	11.5	12.1 ± 0.5	15.5	8.5 ± 0.1	1.0 ± 0.1	0.1	A
NGC 2071	0:20:48	3 → 2	0.12	0.02	12.2	1.1	18.6	9.9	11.9 ± 0.4	17.5	7.6 ± 0.1	1.0 ± 0.1	0.3	
205.11−14.11 0.5[a]		Arc.	598.7	9.6	15.9	−8.0	19.4	5.7		27.4		971.7	9.6[4]	IRAS 05445+0020
12	6: 5:16.9	2 → 1		0.03										(A)
Mon R2(1)	−6 : 22:48	3 → 2		0.04										
213.70−12.62 1.1		Arc.	38.2	2.3	11.8	11.5	12.0	11.8		0.5		27.4	10.7[4]	NGC 2070

A=Anglada et al. (1996); Arc.=Cernicharo et al. (1990), Palagi et al. (1993), Brand et al. (1994); B&E=Braz & Epchtein (1983); B89= Braz et al. (1989); Bro=Bronfman et al. (1996); C=Churchwell et al. (1990); Cha=Chan et al. (1996); C95=Caswell et al. (1995) C96=Caswell (1996); CV95=Caswell & Vaile (1995); E=Ellingsen et al. (1996); G=Gaume & Mutel (1987); Gen=Gensheimer et al. (1996); H=Henning et al. (1992); Hof=Hofner & Churchwell (1996); J=Jenness et al. (1995); Juv=Juvela (1996); M=Molinari et al. (1996); Men=Menten (1991); P=Plume et al. (1992); Sca=Scalise et al. (1989); vdW=van der Walt et al. (1995); WB=Wouterloot & Brand (1989); Z95=Zinchenko et al. (1995)

Distance references: [a] Jennskens & Wouterloot (1990); [b] Brand & Blitz (1993); [c] Avedisova & Palouš (1989); [d] Henning et al. (1990); [e] Simpson & Rubin (1990)

Cloud velocity references: [1] Bronfman et al. (1996); [2] Plume et al. (1992); [4] Anglada et al. (1996); [5] Zinchenko et al. (1995); [6] Juvela (1996); [7] Wouterloot & Brand (1989); [8] Churchwell et al. (1990); [9] Jenness et al. (1995); [10] Wouterloot et al. (1988); [11] Brand & Blitz (1993); [13] Lada et al. (1991); [14] Haschick et al. (1989); [15] Gardner & Whiteoak (1978); [16] Codella & Felli (1995); [17] Cesaroni et al. (1991)

Table B.2. Onsala source catalogue and the observed SiO $J = 2 - 1$ line parameters

No.	Source (l,b) [°] (1)	dist. [kpc]	R.A. Dec. (1950) (2)	Line SiO Cat. (3)	T_A^* [K] F_{peak} [Jy] (4)	rms [K] [Jy] (5)	V_{peak} [km/s] (6)	V_{min} [km/s] (7)	V_{max} [km/s] (8)	V_{cen} [km/s] (9)	V_{mean} [km/s] (10)	FW [km/s] (11)	Width [km/s] (12)	Area [K km/s] S [Jy km/s] (13)	P V_{cloud} [km/s] (14)	Remarks (15)
1	118.96+1.89	3.4	0:11:46.0	2 → 1		0.02									−36.2[1]	UC, (P118.96+1.89), M(NH3)
	IRAS 00117+6412		64:12: 6	(Arc.)		3.5										WB325, Bro
2	121.30+0.66	1.6	0:33:53.3	2 → 1	0.22	0.02	−17.1	−24.0	−10.2	−17.1	−16.6 ± 2.0	13.8	6.8 ± 0.3	1.2 ± 0.1	0.0	Arc., P121.30+0.66, J, Bro
	IRAS 00338+6312		63:12:32	H	0.9		−10.51	−10.9	−10.1	−10.5		0.8		0.7	−17.6[2]	RNO 1B (STAR)
3	122.02−7.08	5.0	0:42: 6.2	2 → 1		0.03										(M)
	J00420+5530		55:30:24	J	0.45		−45								−51.2[3]	
4	123.06−6.31	2.9	0:49:27.8	2 → 1	0.16	0.02	−31.7	−40.3	−23.1	−31.7	−31.3 ± 3.1	17.2	10.0 ± 0.4	1.5 ± 0.1	0.0	(P123.07−6.31), Z94
	IRAS 00494+5617		56:17:28	H	163.1		−36.2	−45.5	−19.8	−32.7	25.7			460	−31.8[2]	NGC 281
5	123.07−6.31	2.8	0:49:29.2	2 → 1	0.11	0.01	−31.3	−36.5	−24.4	−30.5	−31.1 ± 3.0	12.1	6.4 ± 0.2	0.9 ± 0.04	−0.1	A
	NGC 281		56:17:37	Arc.	22.6	1.5	−28.7	−43.0	−13.9	−28.5		29.1		94.1	−30.8[4]	S184, IRAS 00494+5617
6	126.68−0.83	1.3	1:19:58.0	2 → 1		0.02									−15.4[18]	
	S187		61:33: 8	Arc.		3.8										
7	126.71−0.82	1.2	1:20:15.2	2 → 1		0.05										OH, UC, Bro
	IRAS 01202+6133		61:33:10	B90											−13.9[1]	
8	133.69+1.22	4.3	2:21:40.8	2 → 1		0.02										P133.69+1.22, A
	W3 (1)		61:53:26	Arc.	90.7	3.5	−34.3	−52.7	−33.8	−43.2		18.9		553.9	−43.4[2]	
9	133.72+1.22	3.7	2:21:53.3	2 → 1	0.11	0.01	−39.6	−44.8	−32.7	−38.8	−38.9 ± 4.6	12.1	6.6 ± 0.3	0.7 ± 0.03	−0.1	P133.71+1.22, A
	W3 (2)		61:52:20	Arc.	427.9	7.6	−40.5	−52.0	−33.4	−42.7		18.6		1473.0	−38.4[2]	IRAS 02219+6152
10	133.72+1.22	4.6	2:21:55.3	2 → 1		0.03										
	IRAS 02219+6152		61:52:34	H	1060.4		−39.6	−51.7	−13.8	−32.8		37.9		3180	−46.0[11]	W3-IRS5
11	133.75+1.20	3.8	2:22: 6.1	2 → 1		0.02										P133.75+1.20, A
	W3 (3)		61:50:40	Arc.	69.7	3.4	−39.3	−49.4	−30.7	−40.1		18.7		114.3	−39.8[2]	
12	133.94+1.06	4.6	2:23:13.7	2 → 1	0.11	0.02	−45.4	−52.3	−43.7	−48.0	−47.6 ± 8.3	8.6	5.9 ± 0.4	0.6 ± 0.04	0.6	Bro
	IRAS 02232+6138		61:38:46	H	1231.5		−48.8	−70.6	−33.4	−52.0		37.2		3925	−46.4[1]	W3 OH
13	133.95+1.07	4.8	2:23:17.3	2 → 1	0.13	0.02	−46.2	−51.4	−35.9	−43.7	−45.7 ± 8.2	15.5	5.1 ± 0.4	0.8 ± 0.1	−0.3	P133.95+1.07, A, G, Gen
	W3 OH		61:38:58	Arc.	14090	7.2	−48.8	−62.0	−31.2	−46.6		30.8		31750	−47.4[2]	(Men), IRAS 02232+6138
14	132.98+8.48	0.9	2:42:32.0	2 → 1		0.02										
	IRAS 02425+6851		68:51:37	Arc.	20.5	1.3	−14.1	−18.2	−7.4	−12.8		10.8		35.1	−10.4[7]	WB441
15	136.38+2.27	4.2	2:46:11.7	2 → 1		0.02										P136.38+2.27, Bro
	IRAS 02461+6147		61:47:34	Arc.		3.7									−42.2[2]	(STAR)
16	133.40+8.88	-	2:48:34.5	2 → 1		0.02										
	IRAS 02485+6902		69: 2:20	Arc.	12.7	1.7	15.4	9.8	21.6	15.7		11.8		18.4	−89.2[7]	WB453
17	137.07+3.00	5.9	2:54:11.2	2 → 1		0.02										P137.07+3.00, (Bro)
	G137.07+3.00		62: 8:29	Arc.		2.1									−53.2[2]	IRAS 02541+6208 (STAR)
18	138.30+1.56	3.9	2:57:35.6	2 → 1		0.03										Arc., C(NH3,H2O), Bro, Z94
	IRAS 02575+6017		60:17:22	H	1.3		−68.1	−68.8	−67.4	−68.1		1.4		2		AFGL4029, S199, Cha
				C	0.65	0.08	−33.3	−35.8	−30.3	−33.1		5.5		0.8	−38.9[1]	WB463

A=Anglada et al. (1996); Arc.=Comoretto et al. (1990), Palagi et al. (1993), Brand et al. (1994); B90=Braz et al. (1990); Bro=Bronfman et al. (1996); C=Churchwell et al. (1990); Cha=Chan et al. (1996); G=Gaume & Mutel (1987); Gen=Gensheimer et al. (1996); H=Henning et al. (1992); Has=Haschick et al. (1983); Hof=Hofner & Churchwell (1996); J=Jenness et al. (1995); M=Molinari et al. (1996); Mor=Moreira et al. (1995); Men=Menten (1991); P=Plume et al. (1992); WB=Wouterloot & Brand (1989); W&W=Wouterloot & Walmsley (1986); Z94=Zinchenko et al. (1994)

Distance references: [a] Jenniskens & Wouterloot (1990); [c] Avedisova & Palouš (1989); [f] Cernicharo et al. (1985); [g] Braz et al. (1990); [h] Clemens & Barvainis (1988); [i] Genzel & Downes (1977)

Cloud velocity references: [1] Bronfman et al. (1996); [2] Plume et al. (1992); [3] Molinari et al. (1996); [4] Anglada et al. (1996); [5] Zinchenko et al. (1994); [7] Wouterloot & Brand (1989); [8] Churchwell et al. (1990); [9] Jenness et al. (1995); [10] Wouterloot et al. (1988); [11] Brand & Blitz (1993); [12] Fich et al. (1989); [18] Joncas et al. (1992); [19] Haschick et al. (1983); [20] Clemens & Barvainis (1988)

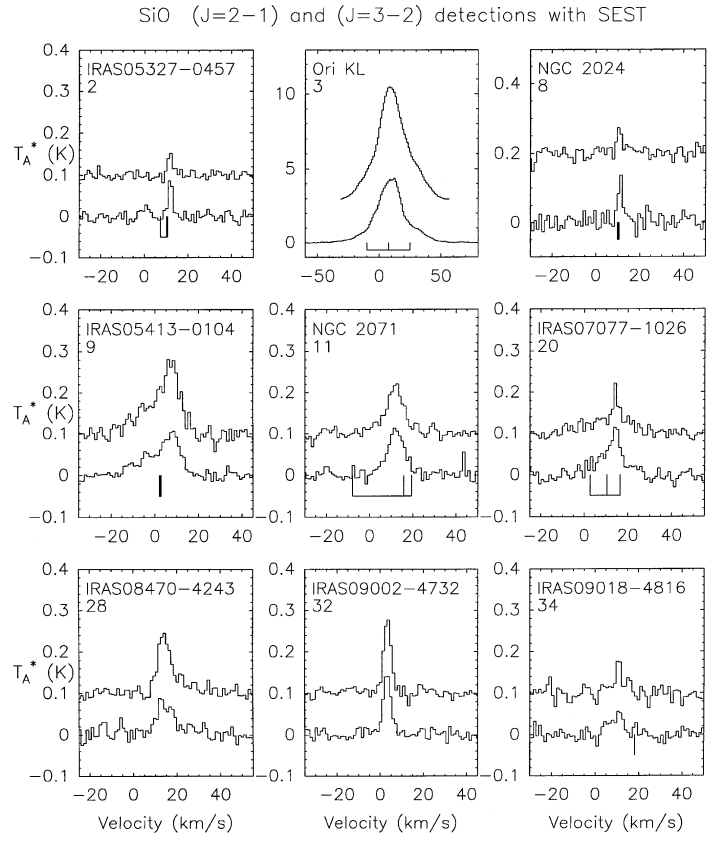
SiO (J=2−1) and (J=3−2) detections with SEST
IRAS05327−0457
2
Ori KL
3
NGC 2024
8
IRAS05413−0104
9
NGC 2071
11
IRAS07077−1026
20
IRAS08470−4243
28
IRAS09002−4732
32
IRAS09018−4816
34
T_A^* (K)
Velocity (km/s)

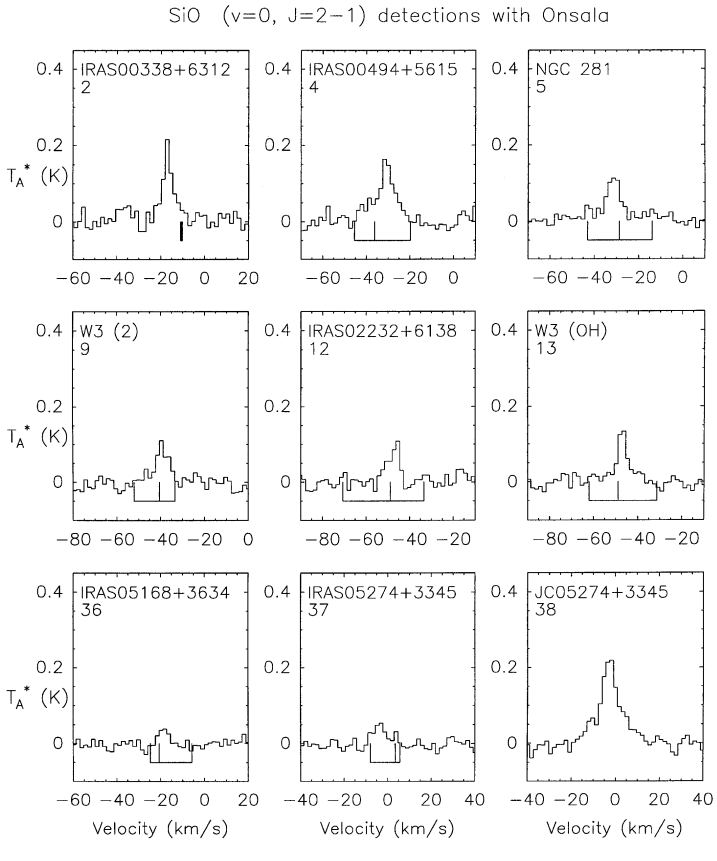
SiO (v=0, J=2−1) detections with Onsala
IRAS00338+6312
2
IRAS00494+5615
4
NGC 281
5
W3 (2)
9
IRAS02232+6138
12
W3 (OH)
13
IRAS05168+3634
36
IRAS05274+3345
37
JC05274+3345
38
T_A^* (K)
Velocity (km/s)